Structural and Photoluminescence Responses of Two-Dimensional Hybrid Perovskite Nanoflakes under UV-Light Illumination

ZHONG CENCHEN

MPhil

The Hong Kong Polytechnic University

2023

The Hong Kong Polytechnic University

Department of Applied Physics

Structural and Photoluminescence Responses of Two-Dimensional Hybrid Perovskite Nanoflakes under UV-Light Illumination

ZHONG CENCHEN

A thesis submitted in partial fulfilment of the requirements for the degree of Master of Philosophy

July 2023

CERTIFICATE OF ORIGINALITY

I hereby declare that this thesis is my own work and that, to the best of my knowledge and belief, it reproduces no material previously published or written, nor material that has been accepted for the award of any other degree or diploma, except where due acknowledgement has been made in the text.

_____ (Signature of Student)

ZHONG Cenchen

_____ (Name of Students)

ABSTRACT

Two-dimensional (2D) organic-inorganic hybrid perovskites have recently emerged as a promising class of optoelectronic materials for various applications, such as solar cells, lasers, and photodetectors. Compared with their three-dimensional (3D) counterparts, 2D perovskites exhibit superior moisture resistance due to their layered structure, wherein inorganic layers are sandwiched by hydrophobic organic layers. Since the optoelectronic applications of perovskite materials often operate under challenging environments involving light exposure, it is crucial to conduct comprehensive studies on the photo-stability of these materials. Until now, the majority of photo-stability studies have been concentrated on 3D perovskites, with limited research on the effect of light on 2D perovskites and the underlying mechanism. Thus, from both application and fundamental standpoints, it is crucial to develop a comprehensive understanding of the influence of light on structure and properties of 2D perovskites. Such knowledge is essential to enhance the longevity of 2D perovskite-based devices and effectively tailor their photophysical properties.

In this work, a type of 2D perovskites with a chemical formula as $(BA)_2(MA)_{n-1}Pb_nBr_{3n+1}$ (n = 1, 2, 3) (BA = butylammonium, MA = methylammonium) was used as a platform to investigate the response of 2D perovskites to ultraviolet (UV) light. Single crystals were synthesized and nanoflakes were prepared by mechanical exfoliation. In the optical microscope, the phenomenon of photobleaching had been observed, where nanoflakes gradually lost their original color and become transparent

in response to UV light illumination. A series of X-ray diffraction and UV-Vis spectroscopy measurement revealed the transition from a crystalline structure to an amorphous structure, accompanied change in optical property of the transparent phase. Fluorescence microscopy was employed to monitor the changes in PL emission. The results clearly demonstrated a blue-to-green redshift in PL emission of the nanoflakes with $n > 1$, which can be attributed to degradation of the pristine crystals and the formation of $MAPbBr_3$ nanoclusters. Additionally, analysis employing electron microscopes confirmed that $(BA)_2(MA)_{n-1}Pb_nBr_{3n+1}$ eventually degrade to $PbBr_2$ under illumination. By utilizing atomic force microscope to measure the thickness of the nanoflakes before and after illumination, it was determined that the reduction in thickness could be attributed to the loss of organic layers. Furthermore, Fourier transform infrared spectroscopy provided evidence of the escape of organic molecules induced by illumination, and the BA molecules were more easily escape than MA molecules which can be attributed to their different locations among layers. It was observed that BA molecules exhibited a higher propensity to escape compared to MA molecules, which can be attributed to their distinct locations within the layers.

This comprehensive investigation provides valuable insights into the mechanism underlying light-induced changes in 2D perovskites and paves the way for the design of photostable optoelectronic applications based on 2D perovskite materials.

List of Publications

Refereed Journal Articles

S. Yan, C. Xu, **C. Zhong**, Y. Chen, X. Che, X. Luo, Y. Zhu, "Phase Instability in van der Waals In_2Se_3 Determined by Surface Coordination". *Angew. Chem.* 2023, 135, e202300302.

Poster Presentation in Conference

C. Zhong, C. Xu, X. Che, C. Yang, C. Chen, Y. Zhu, "Behavior of Two-Dimensional Organic-Inorganic Hybrid Perovskite Nanosheets under Illumination". Chinese Materials Conference 2022-2023, Shenzhen, China.

Acknowledgements

Time slips through my fingers, and a wonderful adventure is about to reach its destination. Looking back on the road I've trod, there are words of gratitude I must express.

First and foremost, I would like to express my sincere gratitude to my supervisor, Prof. ZHU Ye. I am immensely grateful for the extraordinary opportunity he bestowed upon me to become a part of his research group. Being his student is a blessing in my life. Since I am an academic rookie, Prof. ZHU's knowledge appears as towering as a mountain to me. However, this does not impede his approachability to me, as he kindly addressed my naive mistakes with gentle words. He is a role model for me, embodying both an exceptional ability and a peaceful demeanor. This thesis stands as a testament to the transformative influence of his guidance, and I am forever indebted to his profound impact on my intellectual and personal development.

My heartfelt appreciation goes to Dr. Xu Chao, Dr. CHE Xiangli. Without their invaluable hands-on guidance, I would have been unable to acquire such a wealth of knowledge. Their patient and gentle guidance has spared me from many detours on my research journey. It a treasured experience for me to have the privilege of learning alongside of them.

I am grateful to my fellow groupmates and officemates. They are Dr. Guo Xuyun, Dr. ZHAO Guangming, Dr. YAN Shanru, Mr. CHEN Changsheng, Ms. YAO Yunduo, Mr. HU Yezhou, Mr. XU Zhihang, Mr. YANG Chen; and Dr. YOU Huilin, Ms. ZHANG

Jing, Mr. QIU Haifa. Throughout this journey, it has been a great comfort to have all of them by my side. For auld lang syne, my friends.

I wish to acknowledge the brilliant support staffs and scientific officers for their consistent professionalism and invaluable assistance. They are Ms. Yonnie CHEUNG, Ms. Meijei WONG, Ms. Tiffany WONG, Ms. Titus AU, Ms. Mandy WONG, Ms. Vivian WONG, Mr. LAM Kwan Ho, Dr. WONG Hon Fai, Ms. HO Wing Man, Mr. CHAN Tsz Lam, Ms Cecilia CHAN (AP); Dr. Hardy LUI, Dr. Wei LU, Dr. Terence WONG, Ms. Joyce LAU, Ms. Pendy HO (UMF); Dr Gu Yanjuan, Ms. Wan Hoi-ying, Mr. Au Yiu-kwok, Mr. Ho Chi-man (ABCT); Dr. Michael Yuen, Dr. Eva Lau (ULS).

In the symphony of my academic pursuit, my deepest appreciation resonates with the guiding light of the Hong Kong Polytechnic University, where beneath the red brick wall, I embark on a journey to unearth the truth, as I nurture my intellect, seeking wisdom's call.

Last but not least, to my beloved parents, whose unwavering love, unwavering support, and unwavering belief in my dreams have shaped me into the person I am today, and for that, I am forever grateful.

Table of Contents

List of Figures

respectively.

Fig. 4.5 Quasi-in-situ XRD. (a-c) Time evolution of XRD pattern of exfoliated n = 1, 2, 3 flakes under UV illumination; (d) variation of peak intensity fitted by an exponential decay function: $y = Aexp(-x/t) + B$.

Fig. 4.6 PL imaging. (a) Top to bottom of each column: optical images, blue light emitting images and overlap of the previous two images of n = 1 flakes; (b) Top to bottom of each column: optical images, blue light emitting images, and green light emitting images of n = 2 flakes; (c) Top to bottom of each column: optical images, blue light emitting images, and green light emitting images of n = 3 flakes.

Fig. 4.7 PL characterization of n = 2. (a) PL images and (b) spectrum of exfoliated n = 2 flakes under continuous illumination, captured at different time intervals; (c) evolution of non-intrinsic low-energy emission peak position as a function of time (left axis) and intensity ratio of intrinsic emission to low-energy emission (right axis); (d) PL image of a partially covered flake and (e) spectrum of the selected regions.

Fig. 4.8 TEM and SEM characterization. (a) Optical and (b) TEM image of an n = 2 flake after illumination (inserted are SAED of selected regions); (c) radial average peak fitting of SAED for different region on the n = 2 flake and other samples; (d) SEM image of a degraded n = 2 flake and EDX data extracted at three points.

Fig. 4.9 AFM characterization of a thin n = 2 flake under illumination for 30 min. (a) AFM images and (b) sample height profile of the flake before and after illumination.

Fig. 4.10 AFM characterization of a thick n = 3 flake under illumination for 60 min. (a)

AFM images and (b) sample height profile of the flake before and after illumination.

Fig. 4.11 Quasi-in-situ FTIR spectrum of perovskites. (a) FTIR spectrum of $(BA)_2(MA)_{n-1}Pb_nBr_{3n+1}$ (n = 1, 2, 3, ∞) perovskites; (b) evolution of FTIR spectrum of n = 1 under continuous illumination; (c) evolution of FTIR spectrum of n = 2 under continuous illumination; (d) evolution of FTIR spectrum of n = 3 under continuous illumination. (e) FTIR spectrum plot of n = 2 with a wavenumber range of 1250 to 1750 cm^{-1}, and (f) intensity change of the two featured peaks and their ratio.

Fig. 4.12 Peak analysis of ~1480 cm^{-1} featured peak in FTIR spectrum of n = 2. (a) Peak fitting of the ~1480 cm^{-1} peak, where the red peak is considered to correspond to the major hydrogen vibrations in MA, and the blue peak is attributed to the major hydrogen vibrations in BA; (b) the intensity of the peaks corresponding to the two organic molecules varies with the illumination time.

Fig. 4.13 Schematic of UV illumination-induced degradation and formation of 3D nanoparticles.

List of Tables

Chapter 1 Introduction

1.1 Background

Energy serves as a crucial pillar upon which humanity relies for both survival and progress. Historically, fossil fuels, such as coal, oil, and natural gas, have held a prominent position in the global energy landscape. However, as the need for sustainable energy options has grown increasingly urgent, there has been a notable shift towards the exploration and advancement of renewable energy sources, including hydrogen energy, tide energy, and solar energy, etc.

Organic–inorganic hybrid perovskites (OIHPs) are an emerging class of materials which have attracted great attention of both academia and industry for photovoltaic applications since Miyasaka et al. proposed the concept of using $CH_3NH_3PbBr_3$ and $CH_3NH_3PbI_3$ as novel visible-light sensitizers in solar cells in 2009.[1] With a general chemical formula ABX_3, the unique crystal structure and the diversity of the A-site, B-site, and X halide ions endow OIHPs with numerous intriguing properties, including large light absorption coefficient,[2] high charge carrier mobility,[3] long exciton diffusion length[4], tunable direct bandgaps,[5] etc. Studies based on perovskites have created various dimensionality for application in perovskite solar cells (PSCs),[6] light-emitting diodes (LEDs), lasers,[7] photodetectors,[8] and other photoelectric fields.

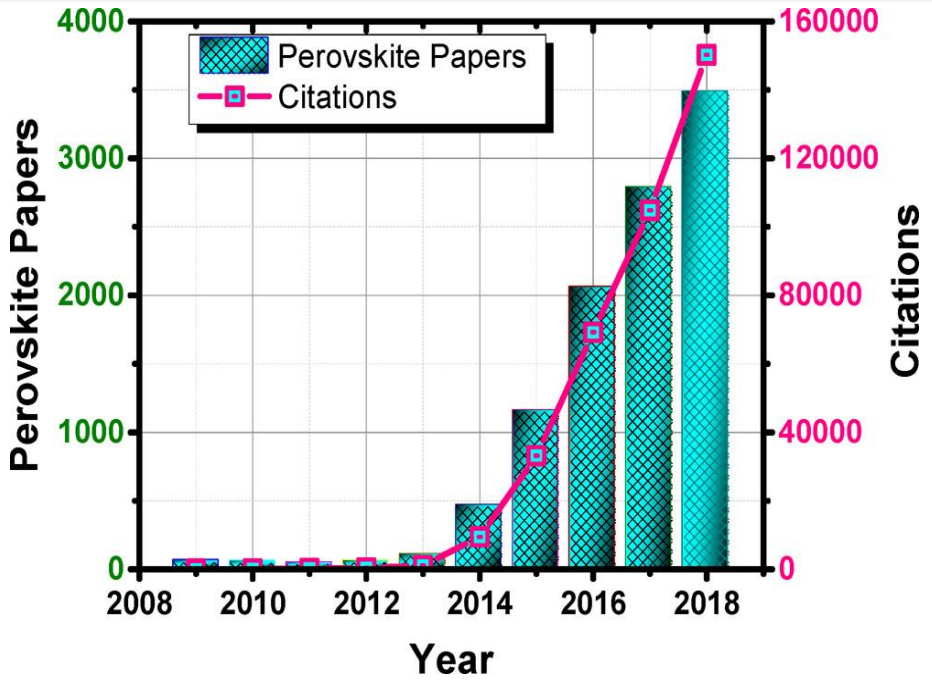

Figure 1.1 Rise of perovskite research as viewed through the published papers and their citation impact during 2009−2018.[9]

However, this material has fatal flaws, one of which is its poor stability especially when exposed to humid environments.[10, 11] This drawback significantly diminishes the operational lifespan of perovskite-based devices in environmental conditions,[12, 13] impeding the commercialization prospects of OIHPs. Employing advanced encapsulating techniques to reduce the permeation of moisture and oxygen in devices is a viable solution,[14, 15] but it comes with drawbacks of high cost and complex processes, and it does not address the fundamental issues related to the structure and properties of the material. To thoroughly address the environmental stability issue of conventional three-dimensional (3D) perovskites, two-dimensional (2D) perovskites have captured the attention of researchers.

The captivating advancements in graphene research have swiftly sparked the

interest and exploration of numerous other 2D materials.[16] By introducing larger cations to A sites, the crystal stacking of perovskite can transition from a 3D bonded structure to a 2D layered structure, facilitated by the weak van der Waals (vdW) forces. The general chemical formula, $(A')_mA_{n-1}B_nX_{3n+1}$, describes the 2D perovskite structure, wherein, the intercalated large cations A' can be either monovalent (m = 2) or divalent (m = 1), residing between the anions within the perovskite sheets; A represents a smaller cation; B represents a divalent metal cation, such as Pb^{2+}, Sn^{2+} or Ge^{2+}; X represents halides, such as Cl^-, Br^-, or I^-; the integer n stands for the number of perovskite layers sandwiched by adjacent large organic molecule layers. Depending on the slight difference in layer arrangement, 2D perovskites can be classified into Ruddlesden−Popper (RP) phases, Dion−Jacobson (DJ) phases, and alternating cation in the interlayer space (ACI) phases. In the layered structure, the organic cations play a crucial role by serving as both insulating barriers, confining the charge carriers within two dimensions, and acting as dielectric moderators that control the electrostatic forces exerted on the electron-hole pairs.[17] The arrangement of alternating organic and inorganic layers create a series of well-defined potential energy barriers and wells, similar to the concept of multiple-quantum-wells (MQWs) structure in traditional semiconductor devices. The MQWs structure enables the manipulation of exciton confinement, leading to high exciton binding energy. In addition to their enhanced environmental stability, 2D perovskites also provide enhanced tunability and flexibility, allowing for precise control over their physical properties. Over the past few years, significant progress has been made in the field of 2D perovskites and in their related optical and optoelectronic devices including solar cells,[18, 19] LEDs,[20, 21] field-effect

transistors (FETs),[22, 23] photodetectors[24, 25] and so on.

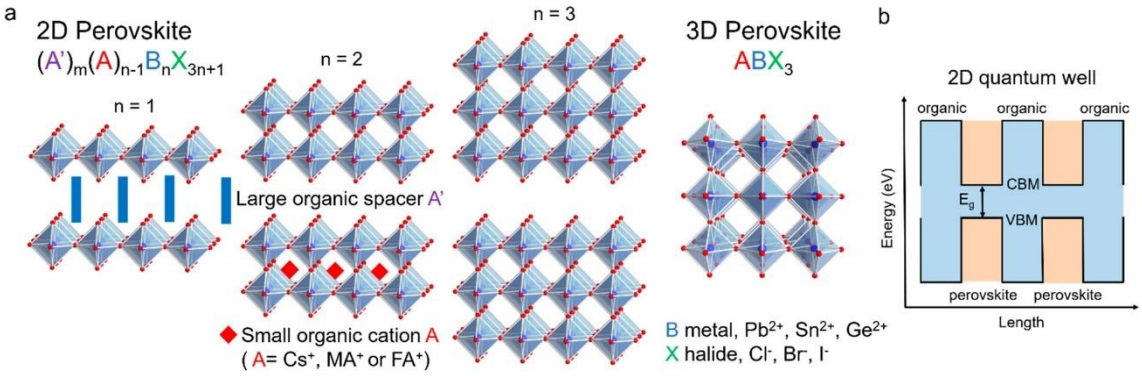

Figure 1.2 (a) Schematic illustration of the evolution from 2D perovskite to 3D perovskite with key components. (b) 2D quantum well structure illustration.[17]

1.2 Objectives of Research

Interest in 2D perovskites has been steadily increasing due to their potential as a more environmentally stable alternative to 3D perovskites. This increased stability is attributed to the presence of interlayered hydrophobic organic cations, which provide resistance to moisture. However, they are still relatively fragile under various external stimuli, including oxygen, heat, light, etc. Most existing studies have predominantly focused on the stability of 3D perovskites, and a comprehensive and consensus-based analysis of that on 2D perovskites is still limited. Particularly, more systematic studies should be involved on the effects of light illumination on 2D perovskites, which is an unavoidable stimulus in the application scenario of these materials. Currently, only few studies focus on the light-induced degradation on 2D perovskite single crystals.[26-29] From both practical and theoretical perspectives, there is an urgent need for a comprehensive analysis of light-induced degradation and modification of 2D

perovskites, and the underlying mechanism.

The broad objective of this study is to investigate the light-induced degradation of $(BA)_2(MA)_{n-1}Pb_nBr3_{n+1}$ (BA = butylammonium, MA = methylammonium, n = 1, 2, 3) 2D Ruddlesden-Popper Perovskites. The ex-situ and quasi-in-situ characterized structural transition process and emission shift phenomenon will significantly advance the understanding of the UV light-induced change of structure and optoelectronic property of 2D perovskites.

1.3 Overview of Thesis

This thesis is comprised of five chapters, which are organized as follows:

Chapter 1: Introduction. The background of organic-inorganic hybrid perovskites from 3D to 2D are introduced. The motivation and significance of this research are explained. Also, the outline of each chapter in this thesis is presented.

Chapter 2: Literature Review. The basic concepts of organic-inorganic hybrid perovskites are briefly reviewed. The structure, property, process, performance of 2D peovskites and their applications are systematically introduced. Subsequently, the alterations in the structure and properties of 2D perovskites under external stimulation, particularly light illumination, are thoroughly discussed. Through a comprehensive review of published literature, this chapter aims to the scientific validity and significance of our research topic, and provides insights and perspectives in conducting research.

Chapter 3: Materials and Methods. The materials and apparatus used in this

research are listed in tables. Various exfoliation methods utilized for the preparation of 2D perovskite samples are discussed. The experiment incorporates a comprehensive range of characterization techniques to provide a thorough analysis. Various techniques such as UV-Vis spectroscopy, fluorescence microscopy, XRD, AFM, FTIR, TEM, and SEM are subsequently described in detail.

Chapter 4: Structural and Photoluminescence Responses of Two-Dimensional Halide Perovskite Nanoflakes under UV-Light Illumination. The synthesis details of 2D perovskite $(BA)_2(MA)_{n-1}Pb_nBr3_{n+1}$ (n = 1, 2, 3) single crystals are presented. The results obtained from diverse characterization techniques utilized to monitor the structural and property alterations of exfoliated nanoflakes under UV light illumination are comprehensively presented. These findings are accompanied by a detailed elucidation of the underlying mechanisms responsible for these observed changes.

Chapter 5: Conclusion and Future Prospect. The comprehensive conclusion of this research study is presented, encompassing both its achievements and limitations. Furthermore, potential avenues for future work in this research field are proposed

Chapter 2 Literature Review

2.1 Introduction

Extensive research has been directed towards hybrid perovskite materials, given their immense potential in photovoltaics and other related fields. Advancements in graphene research have led to a growing awareness of the unique properties that emerge due to the distinctive structure of 2D materials. Possessing both of these intriguing attributes, 2D perovskites have emerged as a captivating class of materials with unparalleled properties and promising applications. Their distinctive arrangement bestows them with unique characteristics and unlocks novel avenues for manipulating their properties. These materials exhibit efficient photoluminescence (PL) and offer tunable emission across a broad spectrum, positioning them as promising candidates for light-emitting devices and optical sensors. Moreover, their exceptional charge transport properties have facilitated the development of highly efficient photovoltaic devices. The structural versatility of 2D perovskites enables their seamless integration into flexible electronics, wearable devices, and transparent solar cells. With their unique structure and properties, 2D perovskites have become a vibrant research area, with ongoing efforts dedicated to unlocking their full potential and overcoming existing limitations.

This chapter provides a comprehensive review of the basic structure and unique properties of 2D perovskites, as well as the recent research progress on this material. We will begin by introducing the traditional 3D perovskites and their existing

drawbacks. Subsequently, this chapter will discuss the structural aspects of 2D perovskites, their unique properties, and the diverse range of applications that have emerged in recent years. A particular emphasis will be placed on examining the stability of 2D perovskites when exposed to various external stimuli. Additionally, the intriguing phenomenon of low-energy state emission exhibited by these materials will be explored. This literature review will serve as a foundation for the subsequent chapters of this thesis.

2.2 Overview of Organic-Inorganic Hybrid Perovskites

Perovskite materials belong to a class of compounds that exhibit the crystal structure found in the mineral perovskite, specifically $CaTiO_3$. This mineral was named after the Russian mineralogist Lev A. Perovski. Perovskite compounds generally have the formula ABX_3, where A and B represent metal cations, and X represents an anion. The first known instance of an organic-inorganic hybrid perovskite (OIHP), methylammonium lead iodide $(CH_3NH_3)PbI_3$ (or $MAPbI_3$), was reported by Weber in 1978.[30] In the case of organic-inorganic hybrid perovskites, at least one of the ions "A," "B," or "X" is organic. Typically, the "A" cation is organic, such as MA^+ (methylammonium) or $CH(NH_2)_2^+$ (formamidinium, or FA^+); "B" represents a metal and "X" denotes a halogen (such as Cl, Br, or I). Space filling ionic size constraints play a crucial role in determining whether a specific group of "A," "B," or "X" ions can form the perovskite framework. This framework consists of a network of BX_6 octahedra that share corners, while the "A" cations occupy 12-fold coordinated voids within the structure to balance the charge of the anions.[31] The structural framework of 3D

perovskites is illustrated in **Fig. 2.1**.

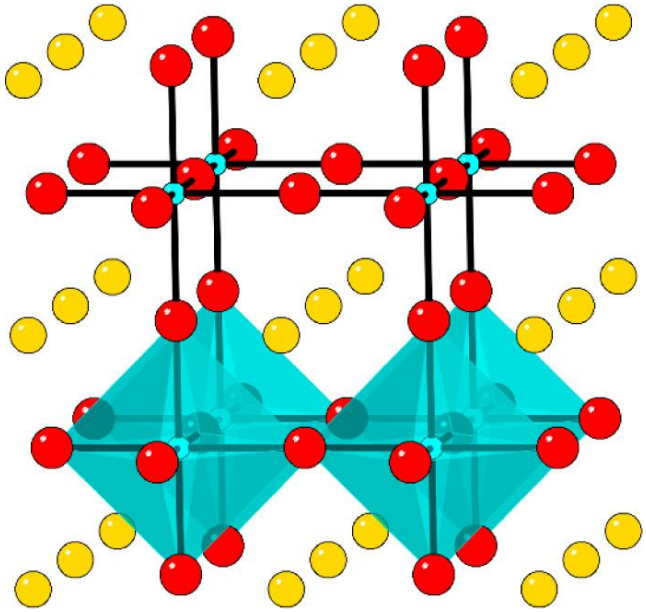

Fig. 2.1 Combined ball-and-stick or skeletal (top) and shaded polyhedral (bottom) representations of the 3D cubic ABX_3 perovskite structure, with A cations filling the voids among the corner-sharing BX_6 octahedra. A, B, and X atoms are shown as gold, cyan, and red spheres, respectively.[31]

The structures of perovskites and their evolution are governed by Goldschmidt's tolerance factor[32]:

$$\tau = \frac{(r_A + r_X)}{\sqrt{2}(r_B + r_X)}$$

where r_A, r_B, and r_X represent the radii of A, B, and X, respectively. A τ value of 0.9–1 is compatible with ideal cubic perovskite structure. When a small A cation or a large B cation is employed, and the tolerance factor falls within the range of 0.7–0.9, the resulting structure typically exhibits an orthorhombic, rhombohedral, or tetragonal

arrangement. For instance, $MAPbI_3$ with $\tau \approx 0.9$, indicating a distorted non-cubic structure that aligns with the experimentally observed tetragonal structure. However, when a large A cation is utilized, the tolerance factor exceeds 1, leading to the destabilization of the perovskite structure. In such cases, layered perovskites are obtained instead.[33]

In 2009, Miyasaka's group made a pioneering breakthrough by utilizing hybrid perovskite as a light absorber in a solar cell, achieving a power conversion efficiency (PCE) of 3.8%. This marked the first successful application of hybrid perovskite in solar cell technology. The widespread attention of the academic community towards perovskite materials began in 2012, when Park, Gratzel, and co-workers first reported on the realization of solid-state OIHP solar cells with an efficiency approaching 10%.[34] This groundbreaking work was considered a milestone in the development of perovskite solar cells. The use of simple and cost-effective solution processes for perovskite preparation highlights the enormous potential of this thin-film solar cell technology as a cost-effective alternative to currently available commercial photovoltaic technologies. In just a decade, the photovoltaic performance of organic-inorganic lead halide perovskite materials has witnessed remarkable advancements, surpassing the top efficiencies achieved by semiconductor compounds like CdTe and CIGS traditionally used in solar cells.[6] Perovskite solar cells have already surpassed the 20% efficiency mark and continue to experience rapid growth, positioning them as strong competitors to similar products within different technological pathways, as shown in **Fig. 2.2**.

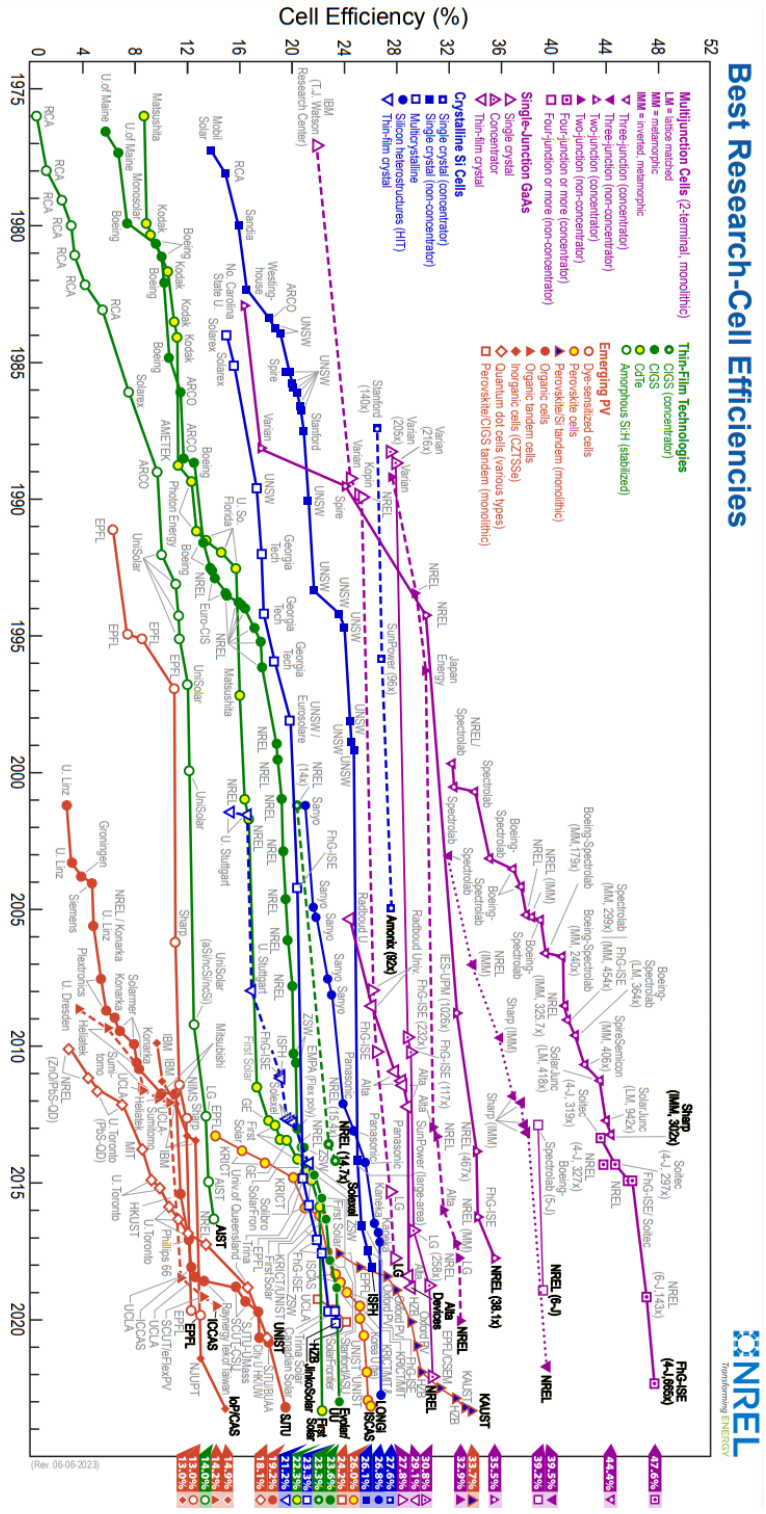

Fig. 2.2 Highest confirmed conversion efficiencies for a range of photovoltaic technologies plotted by National Renewable Energy Laboratory (NREL).

OIHPs not only have potential in photovoltaic applications but also have attracted widespread attention for their exploration in other various optoelectronic applications, as shown in **Fig. 2.3**. For example, solution-processed $CH_3NH_3PbX_3$ (X = Cl, Br, I) has been discovered to possess ultra-stable amplified spontaneous emission at remarkably low thresholds and visible spectral tunability, making them potential electrically driven solution-processed on-chip coherent light sources.[35] Li et al. reported a bottom-gate top contact phototransistors based on mixed-halide ($CH_3NH_3PbI_{3-x}Cl_x$) perovskite films. These phototransistors demonstrated excellent carrier transport properties, displaying ambipolar characteristics, and exhibiting a remarkable response speed of less than 10 μs.[36] Wang et al. presented a photodetector that utilized $CH_3NH_3PbI_3$ perovskite films with an island-structured morphology rather than a compact surface. This unique film structure resulted in improved device performance compared to conventional compact $CH_3NH_3PbI_3$ devices. The island-structured photodetector exhibited a dark current ratio greater than 1×10^4 and demonstrated excellent thermal stability up to 100 °C.[37]

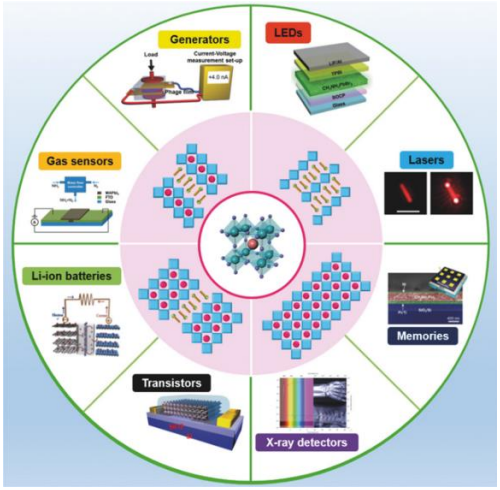

Fig. 2.3 Perovskite-based devices beyond photovoltaics. Including LEDs, lasers, memories, transistors, X-ray detectors, Li-ion batteries, piezoelectric energy generators,

and gas sensors.[38]

The main drawbacks of OHIPs materials are their poor stability and the potential for toxic Pb loss to the environment. The issue of toxicity can be relatively easily addressed, as less toxic/non-toxic elements such as tin and antimony can be potential candidates as alternatives to lead.[39, 40] The structural stability of OIHPs can be assessed using the tolerance factor mentioned earlier in the previous text. During device operation, the electric field can induce intrinsic ion migration and the specific pathways through which ion migration occurs in polycrystalline films of perovskite are currently unknown.[6] Considering the outdoor working environment of solar cells and other devices, the stability under external stimuli like moisture, oxygen, heat, light is a critical issue. Most typically, water molecules readily form hydrates through hydrogen bonding with perovskite, and further infiltration can result in the degradation of perovskite into PbI_2 and other components. OIHPs demonstrate high sensitivity to oxygen, which not only induces degradation but also impacts the PL performance, with the precise extent of this effect still being a subject of debate.[41-44] The impact of light exposure on the material is an unavoidable issue, leading to effects such as ion migration, the generation of low band gap trap states, and phase separation in mixed-halide perovskites.[45-49] Elevated temperatures can also trigger the degradation of OIHPs.[49, 50] To achieve the commercialization of perovskite materials, the issue of stability must be overcome.

2.3 Structure and Synthesis of 2D Perovskites

The discovery of graphene has stimulated renewed interest on various 2D materials, including black phosphorus, hexagonal boron nitride (h-BN), transition metal

dichalcogenides (TMDs), etc. due to their exotic and technologically useful properties that emerge when heat and charge transport is confined to a plane. [16] Reduction in dimension from 3D to 2D provides organic-inorganic hybrid perovskites with better environmental stability and novel optoelectronic properties.[51-53] The stability of 2D perovskites arises the hydrophobic barriers formed by interlayered organic molecules that avoid moisture from penetration. The organic layers with small dielectric constants can act as dielectric layers, which confine the electric field within the inorganic layers, leading to a modified electronic structure. The dielectric confinement effect can affect the exciton binding energy, charge carrier mobility, and other optical and electronic properties of 2D perovskites. Multiple quantum well (MQW) electronic structure is naturally formed is due to the layered sandwich-like structure with organic and inorganic layers alternating arranged, because the dimensions of layers are comparable to the wavelength of charge carriers. This quantum confinement effect leads to discrete electronic energy levels within the band structure. As a result, the electronic properties of 2D perovskites, such as their energy bandgap and charge transport properties, can be tuned by controlling the thickness of the materials. These unique properties are the fundamentals that make 2D perovskites promising materials for a wide range of optoelectronic applications, including solar cells, LEDs, photodetectors, etc.[54-56]

The primary category of 2D halide perovskite compounds comprises corner-sharing octahedra, which can be categorized into three types: structures oriented along the (100) direction, structures oriented along the (110) direction, and structures oriented along the (111) direction. This classification is based on the slicing direction of crystallographic layers along a specific (hkl) plane of the parent 3D structure.[52] The

(100) oriented 2D/quasi-2D perovskite materials can be classified into three types: Ruddlesden-Popper (RP), Dion-Jacobson (DJ) perovskites, and alternating cations in interlayer space (ACI) perovskites. The RP and DJ phases have the general formulas $A'_2A_{n-1}B_nX_{3n+1}$ and $A'A_{n-1}B_nX_{3n+1}$, respectively. The spacer cation in RP is monovalent, while in DJ is divalent. ACI is a relative new phase with a general formula $A'A_nB_nX_{3n+1}$. The crystalline structures of these three phases are shown in **Fig. 2.4**. The octahedral layers in RP phase $(BA)_2(MA)_2Pb_3I_{10}$ have a (1/2, 1/2) in -plane shift. The octahedral layers in DJ phase $(3AMP)(MA)_2Pb_3I_{10}$ are typically perfectly aligned with no relative shift. In ACI, the A-site cation not only resides in the perovskite slab but also fills in the interlayer, and the structure of ACI phase $(GA)(MA)_3Pb_3I_{10}$ has a (1/2, 0) shift.[52, 57]

RP phase 2D perovskites are most commonly studied nowadays. Large-size spacer cations, such as n-butylammonium (BA), phenylethylammonium (PEA), 5-ammoniumvaleric acid (5-AVA) etc. are suitable for RP structure. 2D perovskites with $n = 1$ are regarded as pure 2D structure, while those with $n > 1$ are occasionally referred to quasi-2D. While 2D perovskites have demonstrated enhanced thermal and environmental stability compared to 3D perovskites, recent advancements have focused on enhancing the performance of 2D/3D-based PSCs and other devices. [54-57] This approach presents an opportunity to strike a remarkable balance between the high absorption and efficiency of 3D perovskites and the superior ambient stability of 2D perovskites.

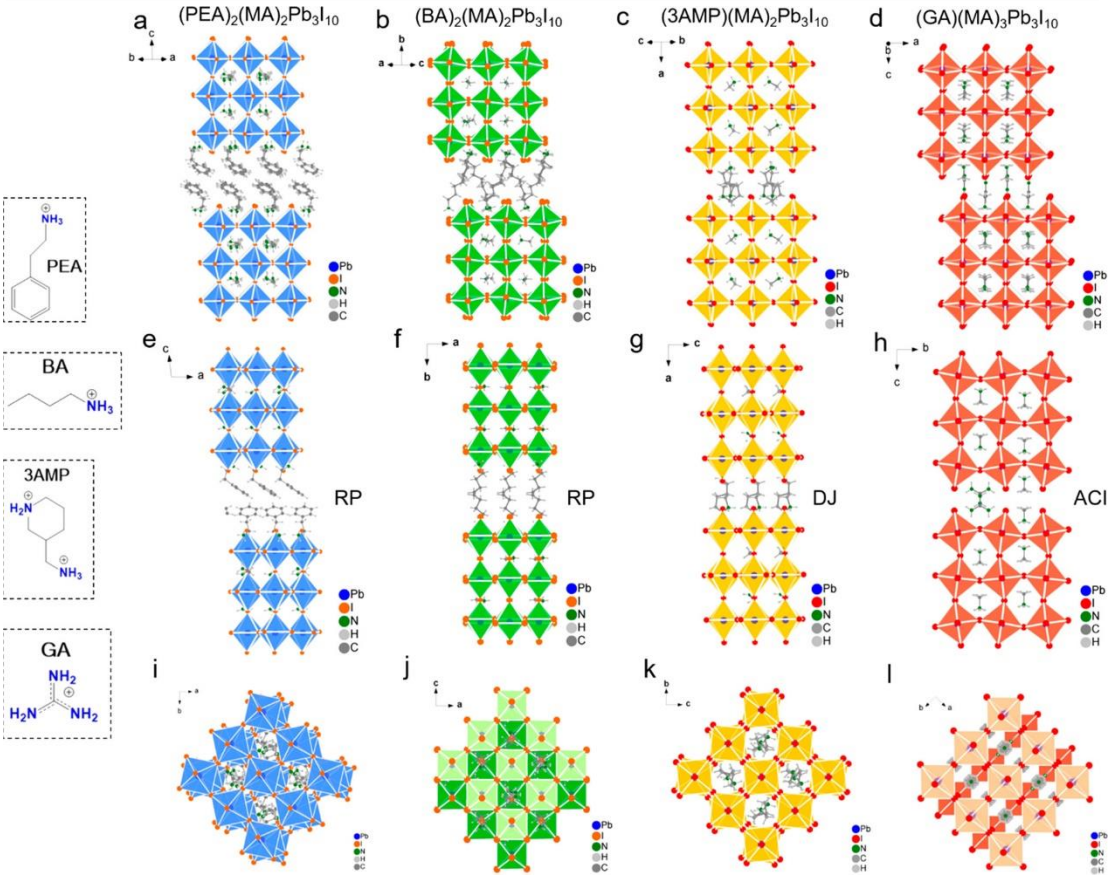

Fig. 2.4 Crystalline structures of RP, DJ, and ACI phases: (a,e,i) $(PEA)_2(MA)_2Pb3I_{10}$; (b,f,j) $(BA)_2(MA)_2Pb_3I_{10}$; (c,g,k) $(3AMP)_2(MA)_2Pb_3I_{10}$; and (d,h,l) $(GA)(MA)_3Pb_3I_{10}$.[52]

For the synthesis of 2D perovskite single crystals, solution-based synthesis methods are commonly utilized. These methods involve the combination of metal halide salt and organic amine in an aqueous acidic solution or the addition of the halide salt of the ammonium cation to an organic solvent containing the metal halide salt.[58] Conventional crystallization methods, such as temperature lowering method, are considerable for synthesis of these materials,[59] wherein saturated precursor solution are cooled from a high temperature in a slow rate, single crystals can be obtained at the solution surface. For example, Stoumpos et al. reported the synthesis of $(BA)_2(MA)_n$-

$_1Pb_nI_{3n+1}$ (n = 1-4) 2D perovskites from a stoichiometric reaction between PbI_2, CH_3NH_3I, and n-butylamine, which is the reaction limiting reagent.[60] Colorful rectangular plates with various layer number n were obtained by precipitation from solution, as shown in **Fig. 2.5**.

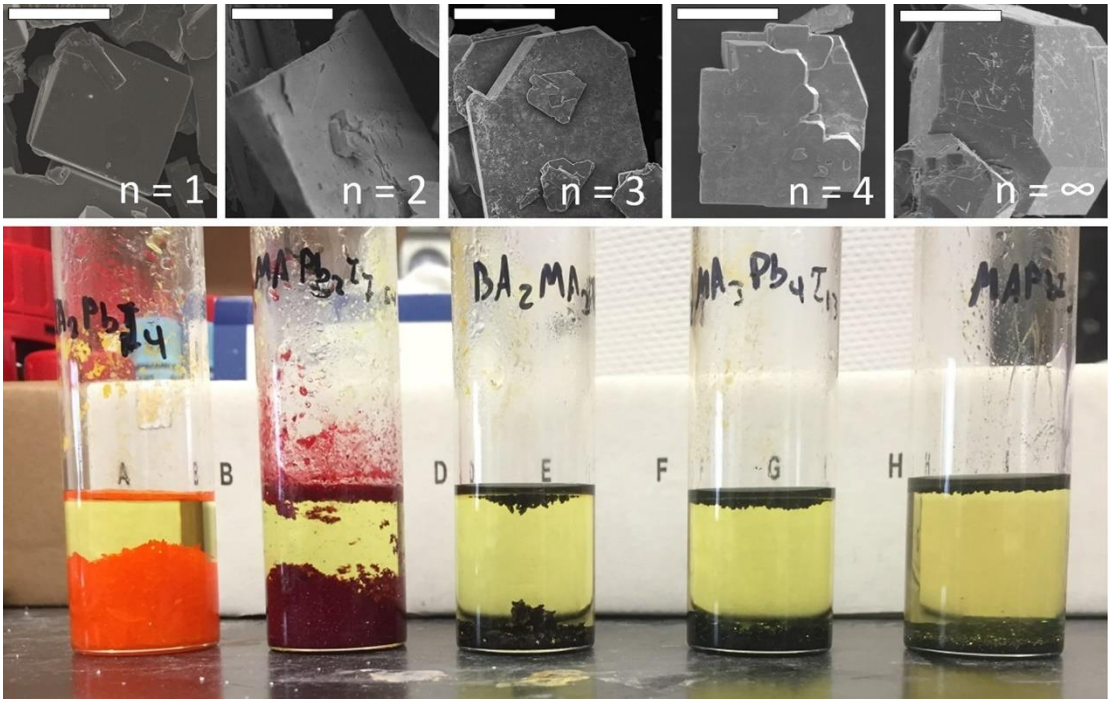

Fig. 2.5 Synthesis of $(BA)_2(MA)_{n-1}Pb_nI_{3n+1}$ perovskite crystals based on solution-state reactions. SEM images (top) and photographs of crystals (bottom) (scale bars = 200 μm).[60]

There are various approaches to prepare ultra-thin crystals, including solution drop-casting method, mechanical exfoliation, epitaxial growth, Interface-confinement growth as shown in **Fig. 2.6**. It is easy to perform drop-casting of a solution onto substrates to form precipitates, but it is challenging to control the thickness and size of the resulting crystals. For example, assembled 2D crystals of $(2T)_2PbI_4$, $(4Tm)_2PbI_4$,

$(4TCNm)_2PbI_4$ and $(BTm)_2PbI_4$ were reported to be prepared by dropping monoammonium-terminated conjugated ligands directly on Si/SiO_2 substrates from a ternary co-solvent.[61] Mechanical exfoliation method widely used in preparation of thin flakes of 2D materials are also suitable for 2D perovskites. The application of this method is detailed discussed in Chapter 3. Epitaxial growth is a technique that allows for precise control over the thickness, size, and orientation of crystalline films or layers. It involves the growth of a thin crystal film on a substrate, where the crystal structure of the film aligns with that of the substrate. Li et al. conducted a study where they synthesized $(BA)_2PbI_{4-x}Cl_x$ microplates by initially synthesizing PbI_2 microplates from an aqueous solution. They then proceeded with intercalation through the vapor transport method and developed microplate-based photodetectors.[62] In the interface-confinement method, the growth of materials at nanoscale are confined between two interfaces, e.g. quartz slides. He et al. reported fabrication of single-crystalline $(BA)_2(MA)_{n-1}Pb_nX_{3n+1}$ (n = 1, 2, 3) films with lateral size reaching millimeter and thickness about 400–1000 nm by dropping precusor solution between two 2×2 μm glass substrates.[63]

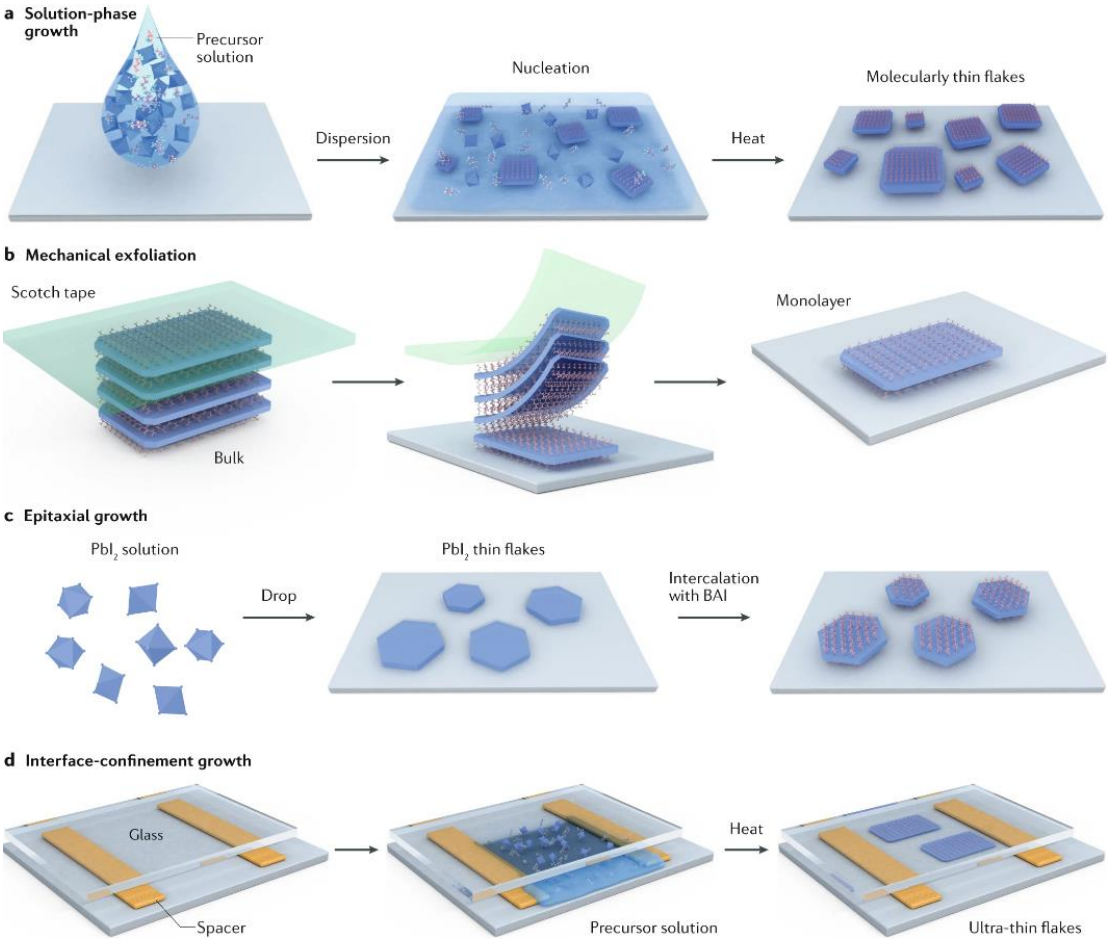

Fig. 2.6 Growth methods for thin 2D perovskite single crystals. a. Solution-phase growth method; b. mechanical-exfoliation method. c. epitaxial-growth method; d. interface-confinement growth method.[53]

2.4 Stability and External Stimulus-Induced Degradation of 2D Perovskites

In contrast to 3D perovskites, which experience significant degradation when exposed to moisture, 2D perovskites demonstrate significantly improved stability and resistance to moisture.[55, 64] However, apart from humidity, 2D perovskites have also been shown to degrade under other conditions. The degradation mechanisms of 2D

perovskites have received less attention compared to their 3D counterparts.

Vacuum stability

Despite the slower degradation compared to ambient conditions, degradation of 2D perovskites cannot be completely avoided under vacuum conditions. Hofstetter et al. demonstrated that as the 2D perovskites are exposed to vacuum for longer durations, the metal lead content increases while the organic content decreases, with the degradation rate depends on the choice of organic cations.[65] Therefore, selecting the appropriate organic cations for two-dimensional perovskites is crucial to prevent degradation.

Thermal-induced degradation

Thermal stress acts as a prominent contributor to the degradation of perovskite devices. Sutanto et al. investigated the response of two representative 2D/3D interfaces to thermal cycles using in situ X-ray scattering techniques.[66] $(2\text{-TMAI})_2PbI_4$ and PEA_2PbI_4 2D perovskite layers with a thickness of about 60 nm were coated on the top of a triple-cation 3D perovskite film to fabricate solar cells. In comparison to 3D-based solar cells, the efficiency of 2D/3D solar cells did not experience a significant reduction following exposure to heat. However, with thermal aging, the crystal structure of 2D perovskite layers on the surface gradually restructured and a mixed intermediate structure is formed at the interface. Fortunately, even in the presence of structural rearrangement at the interface, the underlying 3D perovskite layers were shielded by protective coatings, ensuring the preservation of device performance. However, Fiorentino et al. discovered that after 250 hours of thermal aging at 85 °C in an inert

gas environment, the PEA_2PbI_4 that was originally covering the surface infiltrated into the 3D bulk in the form of PEAI, thereby losing its ability to protect the device.[67] Additionally, under simulated 1 sun illumination, the 2D layers went through a structural transformation from a pure 2D phase to a mixed 2D phase as the film aged.

Electron beam irradiation-induced degradation

As a conventional characterization technique, the use of an electron beam in TEM can also lead to degradation of 2D perovskites. At high energy, the nucleus can be displaced by incident electron beam; at low energy (≈80 keV in TEM), inelastic scattering dominant the induced-damage. Details of these two types of electron-specimen interactions in TEM are discussed in Chapter 3. Jung et al. reported a molecular-scale observations of dynamic surface reconstruction of $BA_2MA_2Pb_3I_{10}$ induced by electron beam.[68] Degradation was induced layer-by-layer with polytypic PbI_2 were found to grow at the edge and surface, as shown in **Fig. 2.7**. They proposed a mechanism similar to the light-induced degradation discussed afterwards. Electron beams, as well as light and heat, have the ability to transfer internal energy to materials, potentially inducing degradation. The PbI_2 formed in this process acted as a shield to protect interior bulk material from degradation.

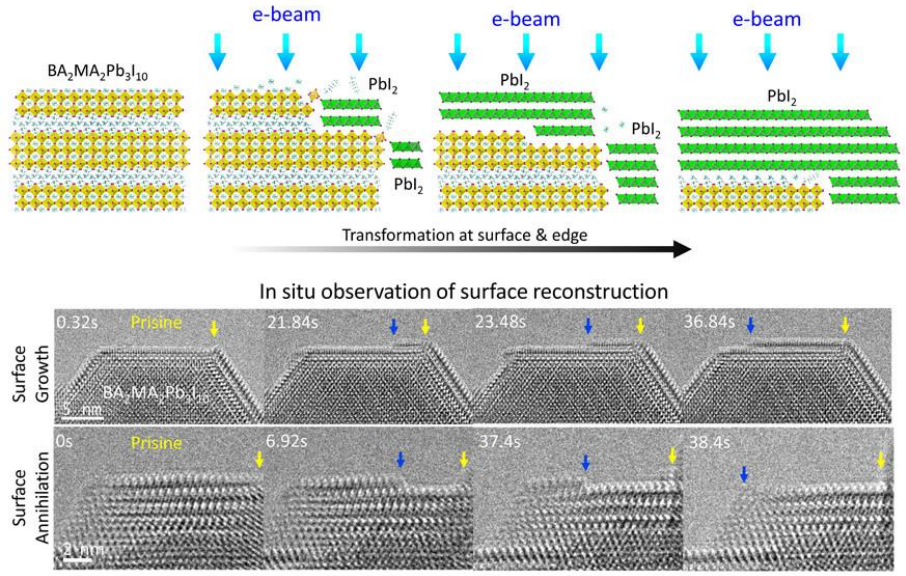

Fig. 2.7 Demonstration of irradiation-induced degradation process and in-situ observation of surface reconstruction of $BA_2MA_2Pb_3I_{10}$.[68]

Light-induced degradation

Light exposure is an unavoidable factor that influences the stability of perovskite materials during usage, making it worthy of investigation. However, there are only limited reports available on its impact on photostability. Fang et al. investigated light-induced degradation of 2D perovskite $(PEA)_2PbI_4$ nanoflakes mechanically exfoliated from single crystals.[26] The sample underwent evident changes under continuous-wave laser irradiation at 488 nm. By measuring the thickness of the flakes through AFM before and after illumination, and comparing it with the thickness contributed by the organic layers in the original lattice, it can be concluded that illumination removes organic molecules from the lattice, leaving behind the PbI_2 layer. Furthermore, prolonged illumination leads to the quenching of PL emission. This can be attributed to the complete transformation of the surface into PbI_2, which has a significantly lower

quantum efficiency. Their observations also indicate that the laser-induced structural transformation at the edges of crystalline flakes occurs at a significantly faster rate compared to the transformation at the surface. They proposed a light-induced degradation process as following, and illustrated in **Fig. 2.8**:

$$(PEA)_2PbI_{4\ solid} \rightarrow PbI_{2\ solid} + [PEA^+ + I^-] \rightarrow PbI_{2\ solid} + PEA_{gas} + HI_{gas}$$

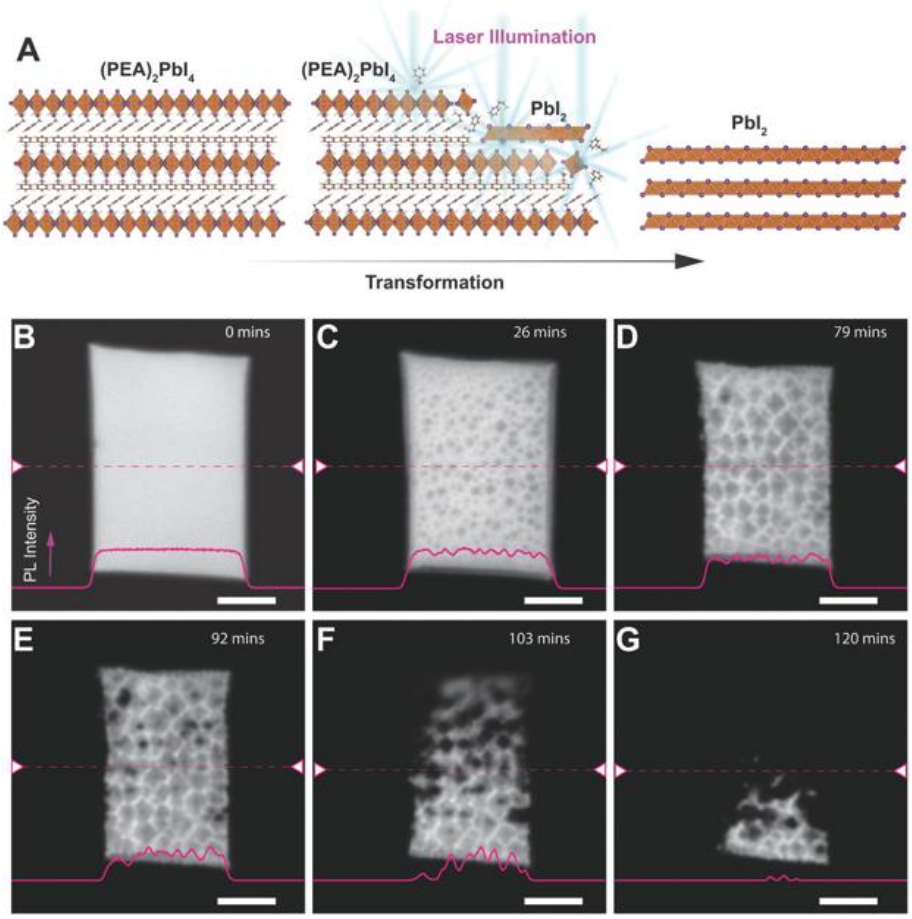

Fig. 2.8 (A) Schematic illustration of the structural evolution from $(PEA)_2PbI_4$ to PbI_2 under resonant excitation; (B–G) confocal microscopy images of a flake at increasing illumination time under a 488 nm laser.[26]

In their study on the degradation of BA_2PbBr_4 nanosheets exposed to UV and white

light, Nie et al. also reported the phenomenon of light-induced degradation occurring from the edges towards the interior by TEM.[27] The perovskite structure remained under light irradiation, with the $[PbBr_6]^{4-}$ octahedral exhibiting ordered tilting. Wei et al. conducted photobleaching experiments and concluded that the photostability of the material was not due to proton exchange photoinduced mechanisms. Instead, they proposed a hypothesis suggesting that degradation occurs through an electrophilic attack of photogenerated halide radicals.[69] Besides RP phase, Zeng et al. studied the light-induced degradation of DJ phase $PDA(FA)_{n-1}Pb_nI_{3n-1}$ films.[70] They proposed a process in which the material undergoes a transformation to generate the three-dimensional counterpart $FAPbI_3$, which subsequently degrades to form PbI_2 under illumination.

In regard to the influence of dimensions on the photostability of 2D perovskites, Udalova et al. proposed that rate of degradation in these materials are nonmonotonically reflected by the layer number n, and for $n \geq 3$, there exist a "stability island", as shown in **Fig. 2.9**.[71] Their work demonstrated that an oxidizing environment played a critical role in light-soaking-induced degradation of prepared films of $BA_2MA_{n-1}Pb_nI_{3n+1}$ with different dimensionalities (n = 1-3) and $MAPbI_3$. The layered perovskites tend to degrade to PbI_2. 2D perovskites were found to degrade faster under illumination with the presence of oxygen than 3D, which could be attributed to the denser 3D framework hindering the penetration of oxygen molecules. Under 450 nm blue LED light-soaking in an inert atmosphere, following stability trend was observed: $n = 3 > n = 2 \approx 3D > n = 1$, extracted from PL spectroscopy. They concluded the difference of underlying mechanisms of degradation induced by heating and light as: thermal degradation can

be primarily attributed to the loss of volatile molecules, while photoelectrochemical reactions is a probable reason to explain the light-induced degradation.

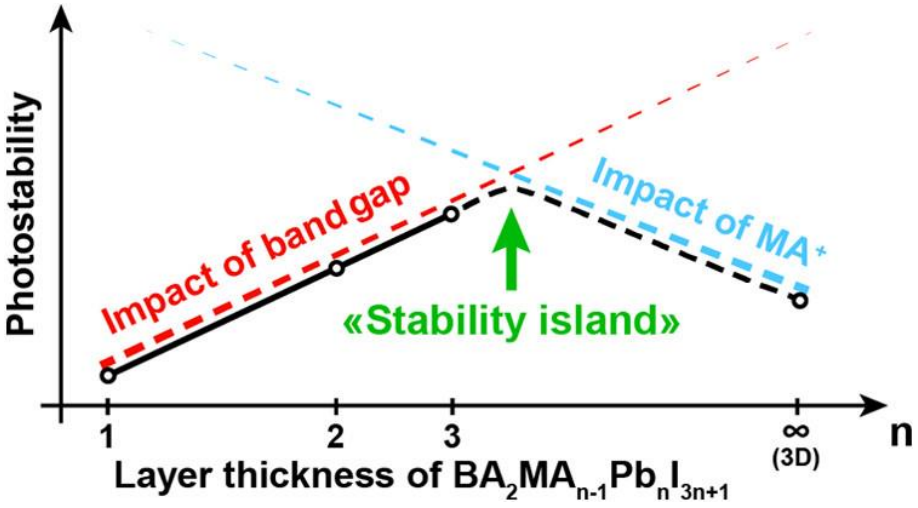

Fig. 2.9 Nonmonotonic Photostability of $BA_2MA_{n-1}Pb_nI_{3n+1}$. This trend could be explained by band gap and higher volatility of MA^+ in MA-abundant compositions.[71]

Chapter 3 Experimental and Characterization Methods

3.1 Experimental Materials

The main materials used in the experiment are shown in Table 3.1.

Table 3.1 Chemical reagents and experimental materials.

Material name	Specification/Purity	Manufacturer
Lead (II) oxide (PbO)	99.9 %	Aladdin
Hypophosphorous acid (H_3PO_2)	50% w/w aq	Aladdin
Hydrobromic acid (HBr)	48% w/w aq	Aladdin
Butylamine hydrobromide (BABr)	98 %	Aladdin
Methenamine hydrobromide (MABr)	98%	Aladdin
N,N-Dimethylformamide	>99.5 %	General-Reagent
Quartz	JGS1	SCDH Tech
KBr	Transmittance > 90%.	Tianguang
AFM tip	EFM-10	Arrow

Silicon wafer	99.999%	Shenzhen Huatepeng
Scotch tape	810D	3M
Thermal release tape	90~100℃	Sunson

3.2 Experimental Apparatuses

The main apparatuses used in the experiment are shown in Table 3.2

Table 3.2 Experimental apparatuses.

Apparatus name	Type	Manufacturer
UVLED light	GHUV-P60UP	GHUV
Optical microscope	DMC 5400	Leica
UV-Vis Spectrometer	Lambda 1050	PerkinElmer
Fluorescence microscope	TCS SP8	Leica
XRD	SmartLab	Rigaku
AFM	MFP-3D	Asylum
FTIR	IS50	Nicolet
TEM	JEM-2100F	JEOL
SEM	VEGA 3	TESCAN

3.3 Exfoliation Methods

Exfoliations of bulk layered 2D materials in mono- or few layer nanoflakes enable the study of their fascinating physical properties related to dimension effect. The weakness of vdW interaction among octahedral layers and organic spacer layers makes it possible to fabricate thin 2D perovskite flakes via mechanical exfoliation method from bulk crystals easily, similar to the cases in conventional 2D materials, such as graphene and transition metal dichalcogenide (TMD).[72]

Mechanical exfoliation method is the most widely adopted method for sample fabrication of 2D organic-inorganic perovskites. Niu et al reported micromechanical exfoliation of hexagonal 2D perovskite $(C_6H_9C_2H_4NH_3)_2PbI_4$ microcrystals to produce monolayers.[73] Yaffe et al produced ultrathin nanosheets of $(C_4H_9NH_3)_2PbI_4$ with lateral dimensions of tens of microns and a thickness of about 2.4 nm onto SiO_2/Si substrates.[74] Li et al adopted mechanical exfoliation method to fabricate 2D Ruddlesden–Popper type perovskite $(C_4H_9NH_3)_2(CH_3NH_3)_{n-1}Pb_nI_{3n+1}$ microplates ($n > 2$) with the thickness of around 20 nm. The flakes were exfoliated on polydimethylsiloxane (PDMS) and positioned on Au electrodes for fabrication of two-probe devices.[75] Guo et al prepared ultrathin $(C_4H_9NH_3)_2(CH_3NH_3)_{n-1}Pb_nI_{3n+1}$ ($n = 1, 2, 3$) flakes by mechanical exfoliated from solution-grown single crystals.[76] Xiong group reported mechanical exfoliation of 2D $(C_6H_5C_2H_4NH_3)_2PbI_4$ ($PhEPbI_4$) perovskite crystals using Scotch tape method.[77] Zhao et al reported exfoliated 2D perovskite $(PEA)_2PbI_4$ (PEA = phenethylammonium) with thickness of about 55 nm used to single-crystal sheet/graphene heterostructure device. Similarly, PDMS stamp was used to transfer 2D perovskite flakes during device

fabrication.[78]

In addition to the mechanical exfoliation, another top-down method, liquid exfoliation, is also applied to prepare 2D perovskite samples. Hintermayr et al. reported a two-step ligand-assisted liquid-phase exfoliation to fabricate $OlA_2MA_{n-1}Pb_nX_{3n+1}$ (OIA = oleylamine, X = Cl, Br, I). The first step is to obtain3D perovskite microcrystals. In the second step, 3D perovskite powder was dispersed in toluene together with ligand OlA and subjected to tip sonication. After centrifugation, nanoplatelets could be obtained in the dispersion.[79] This work provides a versatile approach for the fabrication of colloidal 2D perovskite nanoplatelets.

Although exfoliation methods have drawbacks incompetent for practical manufacturing e.g., bad control of size and thickness of exfoliated flakes, low production yield; it is still a suitable method for laboratory research.

In the experiment of this thesis, the synthesized $(BA)_2(MA)_{n-1}Pb_nBr_{3n+1}$ (n = 1, 2, 3) 2D perovskite single crystals are mechanically exfoliated by Scotch™ tape. Select a single crystal with a thin and flat surface and place it on the tape, then fold the tape several times until the desired flake thickness is obtained. Usually, 3-4 times of tape exfoliation is enough, otherwise the obtained flakes would become fragmented due to the soft lattice of 2D perovskites. The flakes are then transferred on top of target substrates by thermal release tape for subsequent characterization.

3.4 Characterization Techniques

3.4.1 UV-Vis Spectroscopy

UV-Vis spectroscopy is a widely used analytical technique that measure the absorption and transmission of light by molecules in the wavelength range from UV to visible light. The generated spectra that plot as a function of wavelength can provide valuable information about the electronic structure, concentration, and chemical properties of molecules. Generally, a UV-Vis spectrometer works by passing a broad-spectrum light through a sample, selecting a specific wavelength with a monochromator, detecting the transmitted or absorbed light with a photodetector, and recording the resulting intensity as a spectrum.

This technique is often employed to determine the concentration of soluble compounds in solution by using the Lambert-beer Law:

$$A = \varepsilon cL$$

in which A denotes the absorbance of light, ε represents the molar absorptivity which is a constant value for a certain solvent, c is the concentration of light absorbing components in the solution, L represents the path length of light through the solution.

UV-Vis spectroscopy can be employed to estimate the optical band gap of semiconductors, serving as an approximate value for the electronic band gap that is challenging to measure directly. It can also distinguish direct and indirect electronic transition. The bandgap in the absorption spectrum is identified as the point where the absorption starts to rise above the baseline. This particular point signifies the minimum

energy needed for a photon to excite an electron across the bandgap and be absorbed by the semiconductor material. The Tauc plot method is a technique utilized to determine the optical bandgap of a material by analyzing its absorption spectrum, as shown in following equation：

$$(\alpha h\vartheta)^n = B(h\vartheta - E_g)$$

in which α denotes the absorption coefficient, hν is the photon energy of light, B is a constant, the band gap of semiconductors is symbolized by E_g, while n is a constant that depends on the type of electronic transition occurring in the material. Specifically, for direct bandgap materials, n = 2, whereas for indirect bandgap materials, n = 1/2. By plotting the absorption coefficient squared as a function of photon energy and extrapolating the linear region, the bandgap energy can be estimated. It is worth noting that the measured intensity by detector is affected not only by absorbance, but by reflectance and scattering related to the surface roughness of each sample, which can cause a non-zero baseline in spectra.

In the experiment of this thesis, UV–Vis absorption spectra were obtained by PerkinElmer™ Lambda 1050 UV-Vis-NIR spectrometer. Tungsten-halogen and Deuterium were used as light sources for UV and visible range. Samples were prepared by transferred mechanical exfoliated flakes onto quartz plates (1.5×1.5 cm^2) and attached to aperture. The spectrum range was from 250 nm to 800 nm, in step of 1 nm.

3.4.2 Fluorescence Microscopy

The phenomenon of PL emission refers to the emission of light from a material

after it has absorbed photons or other forms of electromagnetic radiation. External photons induce a transition from the ground state to the excited state of a material. As the excited state is generally unstable and short-lived, the material rapidly returns to the ground state, releasing the excess energy in the form of light photons or radiation. PL can be classified into two primary types: fluorescence and phosphorescence. Fluorescence is characterized by a rapid emission of light in the picoseconds to nanoseconds time scale, while phosphorescence involves a much slower emission in the microseconds to thousands of seconds time range. PL finds extensive application in fluorescence spectroscopy, imaging, and microscopy, playing a vital role in the study of biological samples, material analysis, and the characterization of electronic properties. Moreover, photoluminescent materials are utilized in optoelectronic devices such as light-emitting diodes (LEDs), lasers, and sensors, where their ability to emit light is harnessed for various technological advancements.

A fluorescence microscope is an advanced optical microscope that utilizes specific excitation wavelengths and optical components to excite and detect fluorescence emitted by biological or material samples. A typical setup of a fluorescence microscope involves a specific light source, excitation and emission filters, objective lens, dichroic mirror, detector, and imaging software.

In the experiment of this thesis, a Leica™ TCS SP8 microscope was used to obtain PL spectra and images. The excitation beam with a 405 nm wavelength came from a solid-state laser, focused onto the samples by objectives model Plan Apo 10×/0.40, Plan Apo 20×/0.75, and Plan Apo 100×/0.95. The microscope can collect emission and imaging with a spectral detection range from 380 to 800 nm. A Nikon™ Eclipse Ti2-E

live-cell imaging system with 365/385/405/435 nm muti-wavelength illumination was used to capture PL images of flakes by objectives model CFI Plan Fluor 4×/0.13 Dry, CFI Plan Fluor 10×/0.30 Dry, CFI Super Plan Fluor 20×/0.45 Dry. The microscope can image in blue, green, and multi-band emission range.

3.4.3 X-ray Diffraction

X-ray diffraction (XRD) is a rapid non-destructive analytical technique used to study the structure of crystalline materials. It provides information about the arrangement of atoms within a crystal lattice and can help identify the type of crystal structure present in a sample. In XRD, a monochromatic X-ray beam is directed onto the sample at a specific angle, while the scanning, detector rotates around the sample to receive the diffraction from different angles. The X-rays interact with the atoms in the crystal lattice, causing them to scatter. The scattered X-rays will interfere constructively if the path difference between the scattered rays is an integer multiple of the X-ray wavelength. According to the Bragg diffraction condition, given by the following equation:

$$n\lambda = 2dsin(\theta)$$

The angle at which the constructive interference occurs is known as the Bragg angle (θ), and it depends on the spacing between the crystal lattice planes (d) and the X-ray wavelength (λ), and n represents the order of the diffraction. By XRD analysis, we can obtain information about the structure, phase, crystal orientation, and other structural parameters such as average grain size, crystallinity, strain, and crystal defects.

In the experiment of this thesis, a Rigaku™ SmartLab X-Ray Diffractometer with the CuKα X-ray of 0.154 nm wavelength was used to characterize the exfoliated nanoflakes placed on silicon wafer substrates. The experimental setup employed the parallel-beam mode, aligning the divergent X-ray beam emitted by the source into a nearly parallel configuration. Samples were prepared by mechanical exfoliating from bulk crystals and transferred onto silicon wafers (1.0×1.0 cm^2).

3.4.4 Atomic Force Microscopy

Atomic force microscopy (AFM) is an advanced imaging and measurement technique renowned for its high resolution in capturing topographic details of sample surfaces. Unlike optical microscopes that use light, the AFM functions by scanning a sharp tip attached to a cantilever, over the surface of a sample. The tip radius typically ranges from a few nanometers to several tens of nanometers in size. The deflection of the cantilever is meticulously tracked using a laser beam that is directed onto the cantilever and then reflected and detected by a highly sensitive photodetector, which can help convert the laser signal to height information. When the AFM probe embarks on scanning, it approaches the sample surface with remarkable proximity, typically within a few nanometers. As the probe navigates across the sample, the vdW forces exerted by the surface provoke deflections in the cantilever, tracing the up and downs of the surface profile. By continuously monitoring the deflection of the cantilever, a topographic map of the surface with heights down to sub-nanometer can be generated. The probe moves in a raster pattern, gathering height information point by point, as it unveils the fine details of the surface landscape. This powerful tool finds extensive application across a diverse range of scientific disciplines, including biology, chemistry,

materials science, etc. In addition to AFM, there are various kinds of scanning probe microscopy (SPM) distinguished by different interaction between probe tip and the sample surface, and offering unique insights into specific aspects of the sample's properties, including conductive AFM, scanning thermal microscopy (SThM), scanning kelvin probe microscopy (KPM), electric force microscopy (EFM), etc.

There are two main modes for the operation of AFM: contact mode and tapping (AC) mode. In the case of contact mode, the probe tip is in full contact with sample surface, allowing for precise measurements. However, this mode carries the risk of potentially damaging soft samples due to the applied force. On the other hand, the tip is oscillating above surface in tapping mode. A feedback loop is used in this mode to maintain the oscillation at a constant amplitude. The height information can be extracted from the vertical movement of the piezoelectric driver used to generate oscillation. Two types of force exist during the scanning process: the probe tip experience attractive force when it is far away from surface while repulsive force when it is close to the surface. By controlling the setpoint of oscillation amplitude, we can leverage the repulsive forces for high-resolution imaging or utilize the attractive forces for delicate treatment of soft samples.

In the experiment of this thesis, an Asylum™ MFP-3D Infinity scanning probe microscope (SPM) was used to measure the surface topographies and the corresponding height profiles of exfoliated nanoflakes. The AC air topography mode was selected, which is the tapping mode, to minimize the potential surface damage produced by tips during the process of scanning above the soft samples. A $PtIr_5$ coated Arrow EFM-10 tips with a resonance frequency of 75 kHz and a force constant of 2.8 N/m were

employed during the measurements. The scanning rate was 1.0 Hz, and images were taken with a minimum resolution of 256×256 pixel^2. The flakes were prepared by mechanical exfoliation and transferred to SiO_2 coated silicon wafers (1.0×1.0 cm^2).

3.4.5 Fourier-transform infrared spectroscopy (FTIR)

Fourier Transform Infrared Spectroscopy (FTIR) is a powerful analytical technique used to identify and characterize the chemical composition of a wide range of materials. It measures the absorption, transmission, and reflection of infrared radiation by a sample, providing valuable information about its molecular structure and functional groups. With its versatility and non-destructive nature, FTIR has found applications in various fields including chemistry, pharmaceuticals, materials science, environmental analysis, and forensic investigations.

Infrared absorption spectroscopy is a type of molecular absorption spectroscopy that occurs when molecules absorb infrared light due to transitions in their vibrational and rotational energy levels. Molecular absorption of infrared radiation only occurs when the energy of the photons in the infrared radiation precisely matches the energy difference between the molecular vibrational levels. As a result, absorption peaks are observed at the fundamental frequency and harmonic frequencies. Typically, absorption peaks beyond the third harmonic are too weak to be detected. The normal modes of molecular vibrations can be roughly divided into two categories: stretching vibrations and bending vibrations, depending on whether there is a change in bond length.

The working principle of FTIR is as follows: Infrared light emitted from a light source is collimated into parallel beams and enters the interferometer system. After

adjustment by the interferometer, a beam of interfered light is obtained. The interfered light passes through a beam splitter and then through the sample, acquiring an interfered signal containing spectral information, which reaches the detector. The detector converts the interfered signal into an electrical signal. The interfered signal in this case is a function of time, with the x-axis representing the moving time or moving distance of the mirror. This interferogram is sent to a computer via an A/D converter, where the computer performs fast Fourier transform calculations, resulting in an infrared spectrum graph with the percent transmittance of infrared light as the y-axis and wavenumber as the x-axis. The wavenumber represents the number of waves per centimeter and is directly related to the energy of the molecular vibrations. Each functional group in a molecule has a unique set of absorption peaks in the infrared spectrum, allowing for identification and structural analysis of the sample. FTIR can be used for identification of known substances by comparing the infrared spectrum of the test sample with a standard infrared spectrum. The similarity and purity of the compounds can be determined based on the consistency of spectral peak positions, wavenumbers, peak shapes, and other features. Additionally, FTIR can be used to study the effects of physical and chemical changes in a sample, such as phase transitions, reactions, and molecular interactions.

FTIR spectroscopy can be performed using different sampling methods, including transmission, attenuated total reflection (ATR), and diffuse reflectance. Transmission mode involves measuring the transmitted light through a thin film or liquid sample. ATR mode is suitable for solids, powders, and liquids and involves pressing the sample against an ATR crystal to obtain the infrared spectrum. Diffuse reflectance mode is used

for solid samples and measures the reflection of infrared light from the sample surface.

In the experiment of this thesis, FTIR spectra of flakes were measured by Thermo Scientific™ Nicolet™ IS50 FTIR spectrometer in the wavenumber range from 4000cm^{-1} to 500 cm^{-1} with KBr beam splitter. Samples were prepared by transferred mechanical exfoliated flakes onto KBr disk substrate.

3.4.6 Transmission Electron Microscopy

The book written by David B. Williams and C. Barry Carter serves as the foundation for the information presented in this section.[80]

The transmission electron microscope (TEM) has established itself as an ideal tool for structural and compositional analysis under atomic-scale, offering atomic-resolution imaging of specimens, along with various signals collected from sub-nanometer regions. Since the wave nature of electrons was demonstrated, revealing their significantly shorter wavelength compared to visible light, the concept of an electron microscope was proposed. The invention of TEM is in response to solve the problem of the wavelength of visible light limiting the resolution of visible-light microscopes. The Rayleigh criterion, applicable to visible-light microscopes, approximates the minimum resolvable distance as follows:

$$\delta = \frac{0.61\lambda}{\mu \sin \beta}$$

In which λ represents the radiation wavelength for imaging, μ denotes the refractive index featured by the viewing medium, and the semi-angle of the magnifying lens

collection is represented by β. A high-quality visible-light microscope typically achieves a resolution of approximately 300 nm. In contrast, a TEM operated at 100 keV has an electron wavelength of approximately 0.004 nm, as determined by de Broglie's equation:

$$\lambda = \frac{1.22}{E^{1/2}}$$

in which E is the energy of an electron in eV and λ in nm. Incorporating the relativistic effects, accelerating voltage and electron wavelength of a TEM can be correlated by:

$$\lambda = \frac{h}{[2m_0eV(1+\frac{eV}{2m_0c^2})]^{1/2}}$$

in which h represents the Planck' constant (≈ 6.626×10^{-34} N·m·s), m_0 denotes the rest mass of electron (≈ 9.109×10^{-31} kg), e is the unit charge (≈ 1.602×10^{-19} C), c signifies the light speed in vacuum (≈ 2.998×10^{8} m/s), V is the potential drop that accelerate the electrons in the TEM. With electrons having wavelengths even much smaller than the diameter of atoms as radiation, it is no wonder that TEM can achieve unparalleled resolution.

As the electron beam is a form of ionizing radiation, it has the ability to generate a series of secondary signals from the specimen, including secondary electrons (SE), characteristic X-rays, backscattered electrons (BSE), etc. Electron diffraction provides valuable insights into the crystal structure, lattice spacing, and specimen morphology. The diffraction process in TEM also follows Bragg's law, where the incident electron beam can be reflected by atomic planes. The crystal structure does not yield any

observable diffraction information when using a visible-light microscope, primarily due to the comparatively larger wavelength of visible light. Compared with XRD technique, a diffraction pattern obtained through TEM can be directly correlated to the corresponding image of the specimen area. Additionally, the scattering mechanisms of electrons differ from those of X-rays. X-rays undergo scattering primarily through interactions induced by and the electromagnetic field of the incident X-rays. In contrast, electrons experience direct scattering from both electrons and nuclei, without involving a field-to-field exchange. It is worth noting that electrons are significantly more strongly scattered compared to X-rays. By inserting an aperture at the image plane of the objective, it enables the observation of diffraction produced only by a specific region of the crystal on the lower fluorescent screen or camera. This technique is commonly called selected-area diffraction (SAED), enabling the determination of the orientation relationship between distinct crystals or the study of minute particles within larger samples.

The issue of electron beam damage, which can arise from the incident beam, is a problem of significant concern. As a kind of ionizing radiation, a notable consequence of electron beam is its potential to impact both the structure and chemistry of the specimen. Polymers, most organic substances, as well as certain ceramics and metals, are susceptible to damage caused by electron beam. For example, when a polymer or organic-based crystalline specimen is subjected to electron beam, it could undergo a significant decrease in crystallinity, which can be evaluated by observing the diminishing diffraction contrast in the image or the disappearance of sharp spots in the diffraction patterns. Instead, the diffraction spots would blur and followed by

appearance of diffraction rings, indicative of amorphous transistion.

Damage can manifest in one of three primary forms:

1. Radiolysis: Inelastic scattering, primarily caused by electron-electron interactions like ionization, is responsible for breaking chemical bonds in certain materials, such as polymers and alkali halides. It is worth noting that radiolysis s not influenced by heat transfer, so lowering temperature or coating cannot be effectively prevented the specimen. The most effective approach is to prepare thinner specimens to reduce the cross-section for interactions, or utilizing higher voltages.

2. Knock-on damage or sputtering: Knock-on damage refers to atoms displacing in lattice, resulting in the creation of point defects. When atoms are ejected from the surface of the specimen, it is known as sputtering. This kind of damage is directly influenced by the energy of the incident beam and can occur universally when the beam energy exceeds a certain threshold. Interestingly, radiolysis is paradoxically reduced at higher beam energy, while knock-on damage is intensified.

3. Heating: The energy of the electron beam can be absorbed by the specimen and converted into phonon vibrations, which result in the heating of the specimen. This heating effect can be particularly detrimental to polymer and organic samples, especially when the specimen has poor thermal conductivity.

While it is crucial to minimize the negative consequences of electron beam damage in most cases, there are certain situations where we can exploit the damage to facilitate specific transformations. Furthermore, electron damage can be harnessed to simulate

stimulus like light illumination and heat.

In the experiment of this thesis, A JEOL™ field emission TEM JEM-2100F operating at 200 kV was used to capture the bright-field TEM images and SAED patterns of samples. Scotch tape transfer method was used to transfer the thin flakes to copper grids for observation.

3.4.7 Scanning Electron Microscopy (SEM)

SEM is based on the principle of scanning a focused beam of electrons across the sample surface. Similar to TEM, when the primary electron beam interacts with the sample, it generates various signals that can be detected and used to form an image. Secondary electrons (SE) and backscattered electrons (BSE) are usual signal used in SEM. SE are low-energy electrons emitted from the surface of a sample, generated through inelastic collisions between the incident electron beam and atoms. BSE are high-energy electrons that undergo elastic scattering when interacting with the atoms. SE provide information about the topography and surface features of the sample, while he intensity of BSE is related to the atomic number of the elements present in the sample, allowing for compositional analysis and contrast based on elemental variations. SEM offers high-resolution imaging and topographical information, enabling detailed examination of microstructure and surface characteristics.

Energy Dispersive X-ray Spectroscopy (EDX) is often integrated with SEM as a complementary technique to enhance the analytical capabilities of the system. When the primary electron beam interacts with the atoms of the sample, it causes the displacement of inner shell electrons. Subsequently, outer shell electrons transition to

fill these vacancies, emitting characteristic X-rays in the process. Each element has its unique set of characteristic X-rays with specific energies directly related to the atomic number of the element. These X-rays are energy-dispersed and detected using a solid-state detector. By analyzing the characteristic X-rays emitted, EDX provides information about the elemental composition and distribution within the sample. SEM and EDX are powerful techniques used in conjunction to provide comprehensive information about the surface morphology and elemental composition of samples

In the experiment of this thesis, the flake samples were prepared by mechanical exfoliation and transferred onto silicon wafers (1.0×1.0 cm^2) and coated by sputtering gold. SEM images and EDX data were acquired with a TESCAN™ thermionic emission SEM VEGA 3 with EDX detector.

3.5 Materials Synthesis

$(BA)_2(MA)_{n-1}Pb_nBr_{3n+1}$ single crystals were prepared by the temperature lowering method.[59] Considering the different compositions of these crystals, the proportions of raw materials used in the synthesis process varied. For the synthesis of BA_2PbBr_4 (n = 1), Br (0.9 mL) and H_3PO_2 (0.1 mL) were mixed together in a glass vial; BABr (23.1 mg) and PbO (100.44 mg) were added in the mixture. For the synthesis of $BA_2MAPb_2Br_7$ (n = 2), HBr (0.9 mL) and H_3PO_2 (0.1 mL) were mixed together in a glass vial; BABr (23.1 mg), MABr (10.08 mg) and PbO (100.44 mg) were added in the mixture; For the synthesis of $BA_2MA_2Pb_3Br_{10}$ (n = 3), HBr (0.9 mL) and H_3PO_2 (0.1 mL) were mixed together in a glass vial; BABr (23.1 mg), MABr (20.16 mg) and PbO (100.44 mg) were added in the mixture. After the respective proportions of raw

materials have been added, the glass vial was put on a hotplate, and completely clear solutions were obtained after reaction for 2 hours at 110 °C. The temperature was cooled to 80 °C, and further to 55 °C at a rate of 3 °C/min. During this cooling process, crystals gradually precipitated on the surface of the solution. The temperature was kept at 55 °C for 15 minutes and cooled to room temperature at a rate of 3 °C/min. The 3D material ($MAPbBr_3$) with infinite n-value was prepare as film on substrates for reference in different characterization.

3.6 Materials Characterization

The 2D perovskite samples utilized in this study were nanoflakes obtained through the mechanical exfoliation of synthesized $(BA)_2(MA)_{n-1}Pb_nBr_{3n+1}$ (n = 1, 2, 3) single crystals using tape. Multiple characterization techniques were employed to investigate the structure, composition, and properties of these nanoflakes. An optical microscope was utilized to observe the photobleaching process of nanoflakes under illumination, whereby the flakes exhibited a tendency to transition from their initial color to a transparent state; an XRD spectrometer was employed to examine the crystal structure of flakes derived from single crystals, as well as to analyze the quasi-in-situ change in crystallinity of the flakes under illumination; a UV-Vis spectrometer was utilized to analyze the quasi-in-situ change in absorption properties of the flakes under illumination; a transmission electron microscope (TEM) integrated with selected area electron diffraction (SAED) was utilized to examine the diffraction pattern of the flakes before and after illumination; the alterations in surface morphology and height profile of the flakes were examined employing atomic force microscopy (AFM) both before

and after illumination; the change in composition of the flakes under illumination was investigated using Fourier-transform infrared (FTIR) spectroscopy; to capture the PL images and spectrum of the flakes, fluorescence microscopes were employed; lastly, scanning electron microscopy (SEM) in conjunction with energy-dispersive X-ray spectroscopy (EDX) was utilized to evaluate the morphology and changes in composition of the flakes subsequent to illumination.

All experiments described in this paper involving continuous UV light illumination of the materials were performed using the same UV LED lamp with a wavelength of 365 nm as the light source, unless otherwise specified. Furthermore, the power of the light source and the vertical distance from the light source directly above the sample surface were kept consistent in all experiments to ensure consistency and comparability of the results. The approximate irradiance is 2000 W/m^2, which is about 2 times of that of Air Mass 1.5 Global solar spectrum AM1.5G (1000 W/m^2). We believe this is an appropriate duration to simulate the state of materials in real-world application environments, while also keeping the duration of individual characterization tests within a feasible range.

Chapter 4 Structural and Photoluminescence Responses of Two-Dimensional Hybrid Perovskite Nanoflakes under UV-Light Illumination

4.1 Introduction

Recently, 2D organic-inorganic hybrid perovskites, particularly Ruddlesden-Poper (RP) type perovskites, have recently emerged as a promising class of optoelectronic materials for various applications, including light-emitting diodes (LEDs), solar cells, lasers, and photodetectors.[81] The RP phase layered perovskite has the general chemical formula of $A_nA'_{n-1}B_nX_{3n+1}$, where A represents a large organic cation such as phenylethylamine (PEA^+) or butylammonium (BA^+); A' represents a smaller cation, such as such as Cs^+, formamidinium (FA^+) or methylammonium (MA^+); B represents a divalent metal cation, such as Pb^{2+} or Sn^{2+}; and X represents halides, such as Cl^-, Br^-, or I^-; n is an integer that stands for the number of corner-sharing $[BX_6]^{4-}$ octahedra layers sandwiched by adjacent organic layers. When n is infinite, the structure becomes a 3D perovskite. When n = 1, 2, 3, and so on, the layered structure with conductive inorganic atomic layers isolated by the insulating organic long-chain molecule layers constitutes an ideal quantum well, leading to large exciton-binding energies, short

exciton-decay times, and other novel properties. Compared with their 3D counterparts, 2D perovskites exhibit superior moisture resistance due to inserted hydrophobic organic layers, which can protect the perovskite crystals from erosion of moisture and further enhance the performance of devices. For example, there have been various report about 2D/3D mixture solar cells with enhanced efficiency and lifetime.[82-84]

Although 2D perovskites have been proposed as more environmentally stable alternatives to their 3D counterparts due to their resistance to moisture, a comprehensive analysis of their photostability is limited. Light-induced modification and degradation will be a more severe drawback for the commercialization of perovskite solar cells. Early studies primarily focused on stability issues, including light-induced degradation and transition, of 3D perovskites, with their mechanisms being highly debated.[85] The light-induced degradation of two-dimensional layered perovskites remains elusive. With the advancement of 2D perovskites and their photovoltaic devices, there is an urgent need for research on the behavior of 2D perovskites under illumination.

4.2 Results and Discussion

The crystalline structure and images of synthesized single crystals of $(BA)_2(MA)_{n-1}Pb_nBr_{3n+1}$ with n = 1, 2, 3 are illustrated in **Fig. 4.1**. The integer value n in chemical formula is used to denote the quantity of perovskite layers sandwiched between two long-chain organic molecular layers. In the case where n = 1, the $[PbBr_6]^{4-}$ octahedrons are spaced apart solely by BA molecule interlayers, without the presence of MA molecules. This arrangement signifies that only BA molecules are present

between the octahedral layers. Conversely, for n = 2 and 3, MA molecules are interspersed within the octahedron layers, indicating that the octahedral layers contain both MA and BA molecules. When n approaches infinity (n = ∞), the 3D counterpart known as $MAPbBr_3$ is formed. `Due to the weak vdW force between the BA organic chains, these crystals can be easily peeled into thin layers using mechanical exfoliation techniques. Consequently, these thin layers can then be transferred onto alternative substrates to facilitate further examination and characterization of their properties. This unique characteristic of easy exfoliation and transferability opens up possibilities for investigating the properties and behaviors of these materials on different substrates, enabling enhanced control and exploration of their potential applications. The synthesized single crystals are prone to breakage and typically have sizes ranging from a few millimeters. It could be observed that the original color of the samples with n = 1, 2, and 3 ranges from white to yellow and deep yellow. This difference in color is attributed to the quantum confinement effect resulting from their distinctive Ruddlesden-Popper structure, which can lead to a gradual decrease of the bandgap as the value of n increases.[60]

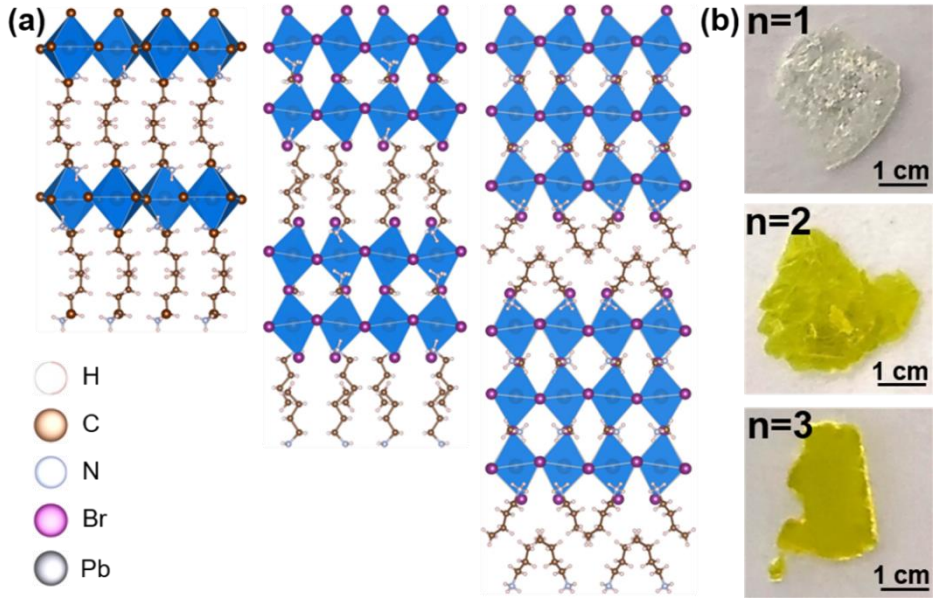

Fig. 4.1 Crystalline model and synthesized crystals. (a) Demonstration of crystalline structure of n = 1, 2, 3; (b) images of synthesized single crystal with size of micrometers.

To verify the purity and quality of the synthesized n = 1, 2, 3 single crystals, some flakes were exfoliated onto silicon wafers for XRD analysis, and the results are shown in **Fig. 4.2**. The periodic diffraction peaks imply that these samples are 2D layered crystals with specific interlayer spacings and orientation. For n = 1, the peaks were at around 2θ = 6.4°, 12.8°, 19.3°, etc., which could be assigned to the (200), (400), (600), etc. lattice planes; for n = 2, the peaks were at around 2θ = 9.04°, 13.56°, 18.1°, etc., which could be assigned to the (400), (600), (800), etc. lattice planes; and for n = 3, the peaks were at around 2θ = 6.96°, 10.42°, 13.9°, etc., which could be assigned to the (400), (600), (800), etc. lattice planes. Few weak peaks observed near the main peaks in the experimental XRD spectrum can be attributed to the presence of the k-α 2 wavelength in the incident X-ray beam. The agreement in the featured peaks between the experimental diffraction spectrum and XRD spectrum calculated based on the

crystal model confirms the high purity of the synthesized single crystals, making them suitable as a basis for conducting further experiments.

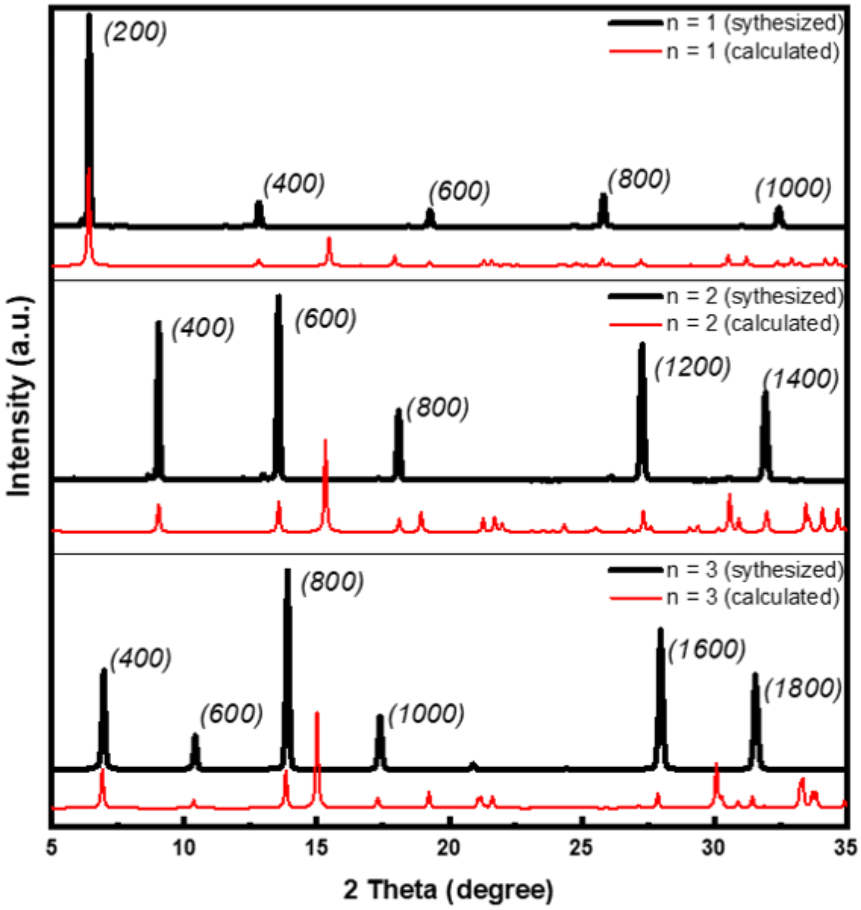

Fig. 4.2 XRD spectrum. Each window contains two plots: a black plot representing the experimental XRD spectrum for synthesized samples, and a red plot representing the calculated diffraction spectrum based on the crystalline model of n = 1, 2, 3.

The most straightforward way to observe the effects of UV illumination on the these 2D perovskites is through optical microscopy. Nanoflakes were mechanically exfoliated on to glass substrates for observation. **Fig 4.3a** illustrates the progressive images of the samples captured under continuous UV light illumination at 0 min, 15 min, and 30 min. Optical microscopy operated in transmission mode. The variations in

brightness and contrast in the image of the n = 1 flakes, as well as the different colors observed in the n = 2 and n = 3 flakes, are attributed to the differences in thickness of the exfoliated samples. This phenomenon is known as optical interference and is commonly observed in 2D materials.[86] When incident light interacts with these materials, it undergoes multiple reflections and interference between different layers. The interference leads to variations in brightness and different colors, depending on the thickness of the samples. Thicker samples may exhibit enhanced brightness or more intense colors, while thinner samples may appear dimmer or display different colors due to constructive or destructive interference. After being exposed to illumination for 15 minutes, the flakes undergo a transition from their original color to a transparent phase, particularly those that are smaller in size and thinner in thickness. It is worth noting that despite the transformation in color, the overall shape and outline of the flakes remain intact. Upon 30 minutes of illumination, most flakes transition into a transparent phase, with only a few large and thick flakes retaining their original color. This change from colored to transparent can be attributed to the significant impact of UV light on the electronic structure of 2D perovskite materials, which alters their absorption of visible light. The loss of color observed in 2D perovskites when exposed to UV light in similar to the phenomenon of photobleaching, where the illumination causes photon-induced chemical modifications or structural changes. This suggests that the degradation of light-sensitive organic molecules leads to modifications in the quantum well structure, ultimately resulting in alterations in the optical properties.

Fig. 4.3b shows magnified images of selected flakes from a large quantity of n = 1,2,3 flakes, illustrating the evolution of their color and morphology over time under

illumination. It is evident that the shape of the flakes remains unaffected by the light exposure. From the n = 1 flake, it can be observed that the contrast transitions from uniform to non-uniform and then back to uniform, indicating a change in its original ordered layered structure due to the influence of light. Interestingly, in the selected flakes of n = 1 and n = 2, there appears to be a gradual loss of color from the edges towards the interior. While in the case of the selected n = 3 flake, the loss of color seems to occurs along the diagonal direction. This could be related to uneven thickness of that flake, as thinner samples tend to have a faster response to light. Due to the inherent randomness in the morphology, thickness, and size distribution of flakes prepared through mechanical exfoliation, various forms of color change trends have been observed across different samples.

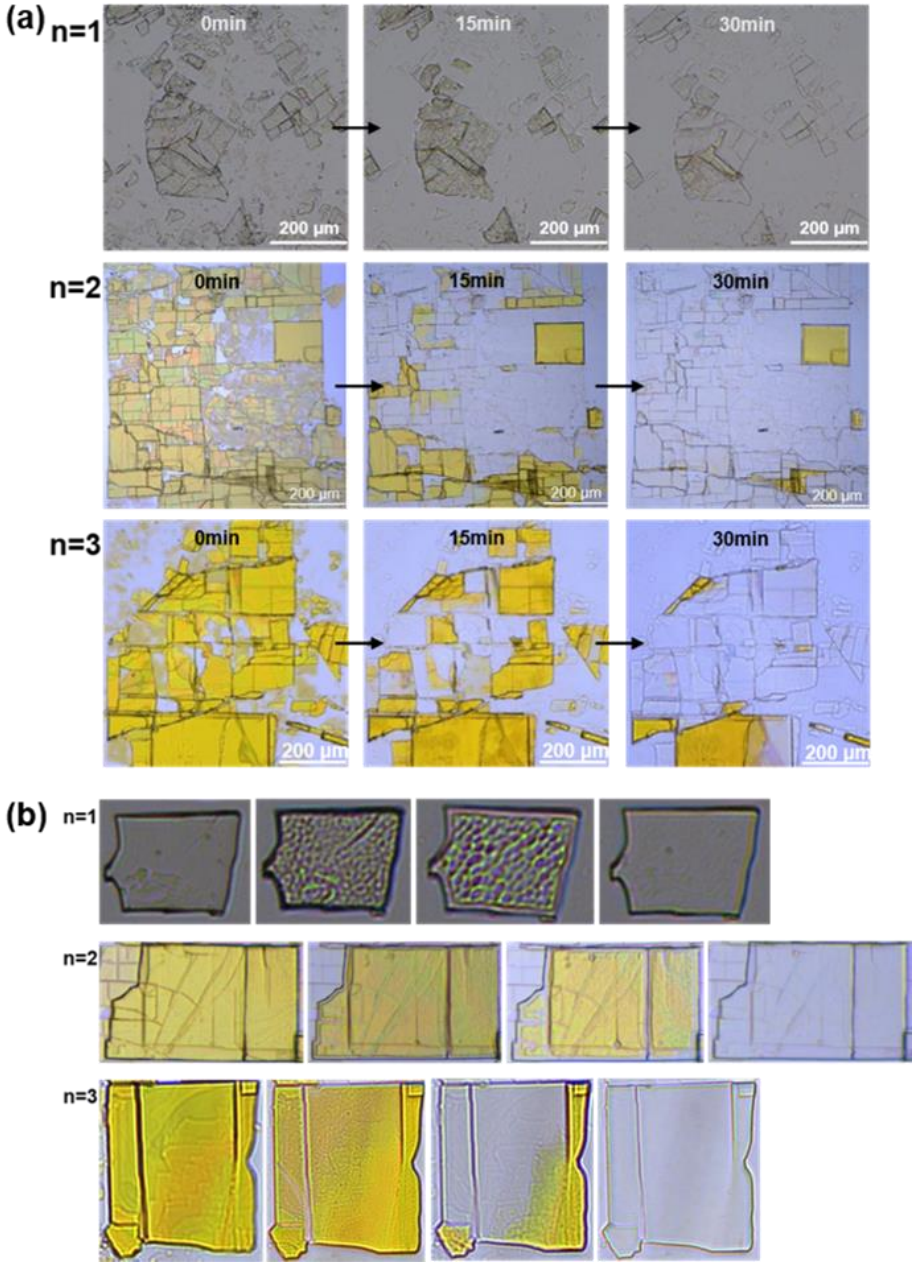

Fig. 4.3 Optical microscopic imaging. (a) Images of exfoliated flakes with n = 1, 2, 3 under UV illumination for 0 min, 15 min, 30 min; (b) selected flakes under illumination over time.

To investigate the phenomenon of color change, the flakes were characterized by quasi-in-situ UV-Vis spectrometry, as depicted in Fig. 4.4. The absorption peaks for n

= 1, 2, and 3 are located at 405 nm, 436 nm, and 458 nm, respectively. By Tauc plot analysis, the bandgap of n = 1, 2, 3 are approximately determined as 2.97, 2.79, 2.60 eV, respectively. This variation is consistent with the gradual decrease in bandgap observed with an increasing value of n.[60] The increase in interlayer spacing among layers leads to weaker quantum confinement effects, ultimately resulting in a reduction of the bandgap. With continuous UV illumination, the absorption peaks of n = 1, 2, and 3 gradually weaken and eventually disappear, without the emergence of any new absorption peaks. Moreover, after several minutes of UV exposure, the final absorption spectra of these samples exhibit similar absorption edges. This suggests that despite differences in composition among the three samples, their compositions should be similar when they are completely transformed into the transparent phase under UV light, resembling $PbBr_2$.[87]

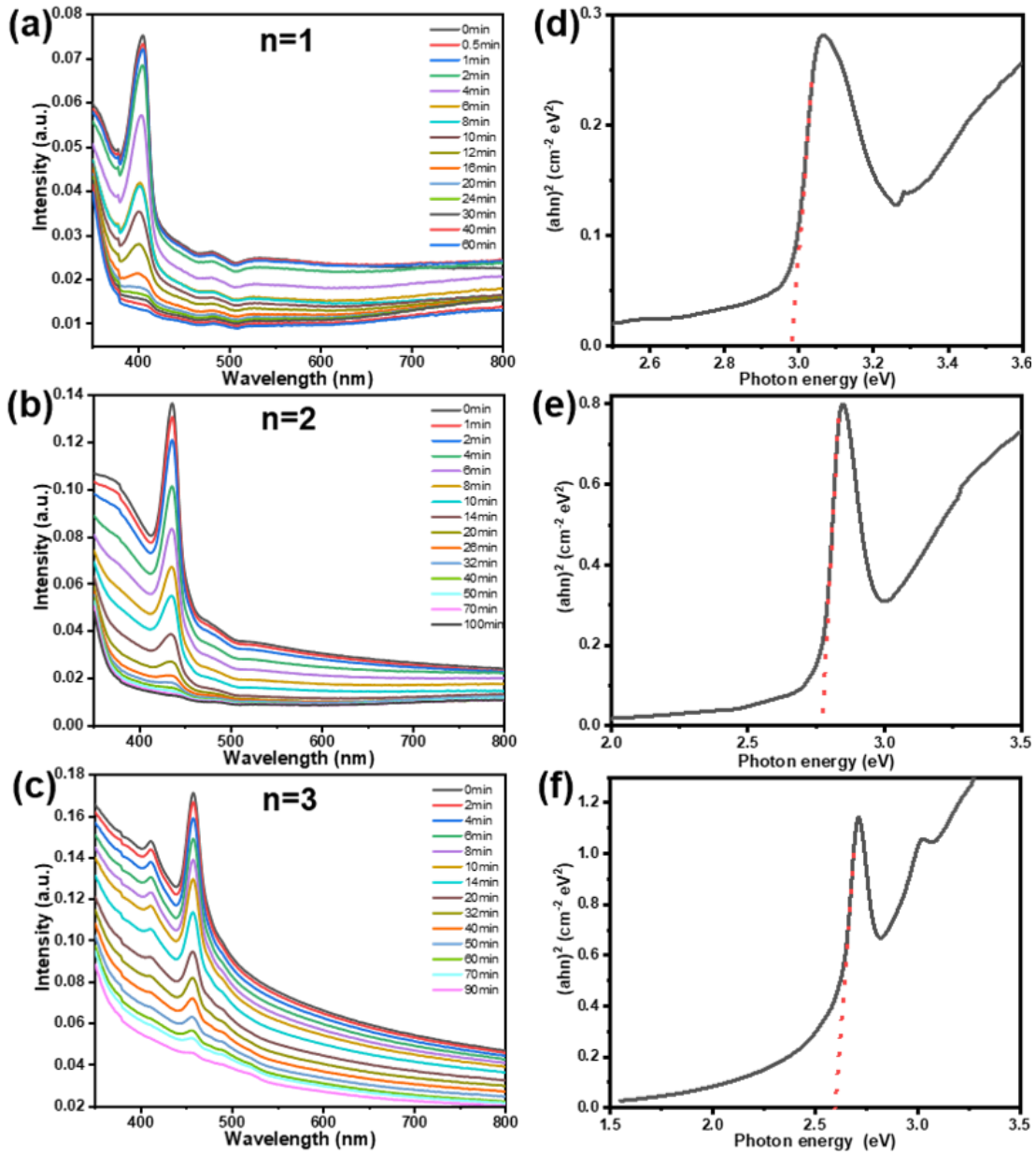

Fig. 4.4 UV-Vis spectrum. (a-c) Absorption spectrum of n = 1, 2, 3 flakes under UV illumination over time; (d-f) Tauc plots derived from each initial absorption spectra, respectively.

To study the crystal structure changes during the illumination process, the flakes were characterized by quasi-in-situ XRD technique, as shown in **Fig. 4.5**. The general

diffraction peak intensity of n = 1, 2, 3 samples signally decrease under UV illumination, which indicates that the interaction between the UV light and the materials has a disruptive effect on their crystal structures. In addition, the absence of any distinct diffraction peaks suggests that no detectable variations in the crystalline structure occurred and that the remaining transparent phase is amorphous in nature. To compare the degradation rates of these materials, we extracted the intensity variations of the strongest peaks from these three XRD patterns as a function of illumination time and fitted the trends using a decay function. The comparison reveals that the n = 1 samples exhibit the highest degradation rate, whereas as the value of n increases, the $(BA)_2(MA)_{n-1}Pb_nBr_{3n+1}$ 2D perovskites demonstrate a gradual improvement in their durability to UV light. The UV light source used in the experiment had a wavelength of 365 nm, which is closer to the characteristic absorption wavelength of n = 1. This may partially contribute to the faster degradation of n = 1. However, considering that the light-sensitive components are the organic molecules within the structure, and n = 1 has the highest proportion of organic content with the least number of sandwiched inorganic layers, this trend is plausible.

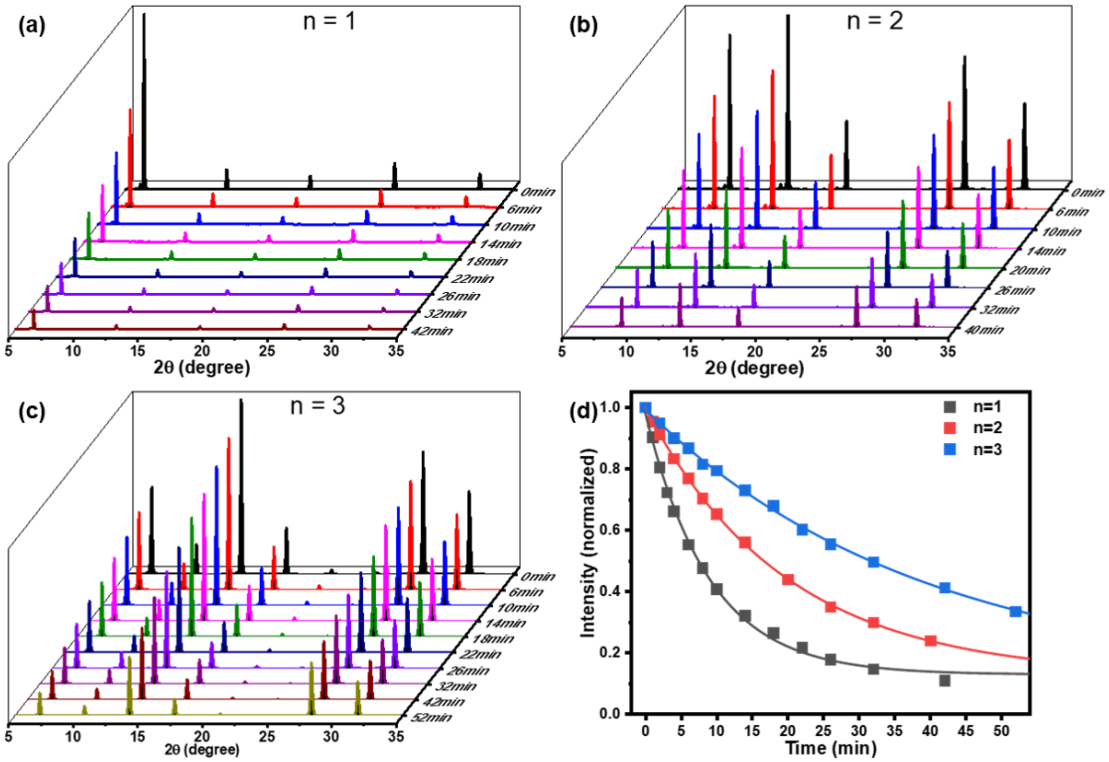

Fig. 4.5 Quasi-in-situ XRD. (a-c) Time evolution of XRD pattern of exfoliated n = 1, 2, 3 flakes under UV illumination; (d) variation of peak intensity fitted by an exponential decay function: $y = Aexp(-x/t) + B$.

2D perovskite crystals can exhibit efficient PL emission, which undergoes changes in response to UV light illumination, concurrent with light-induced degradation. **Fig. 4.6** showcases the optical and PL images obtained by a fluorescence microscope. The wavelength range of blue light falls between 435 and 485 nm, which is comparable to DAPI, a common blue fluorescent dye; and the range of green light is between 500 and 550 nm, resembling the wavelength range of FITC, a common green fluorescent dye. It is worth noting that in this study, we utilized the built-in light excitation light source of the fluorescent imaging system to provide UV irradiation. This means that the irradiation method is different from the approximate parallel light used in other

experiments in this chapter. Instead, it involves scanning a smaller diameter point light source emitted from the microscope onto the samples. From the optical images, it can be observed that due to the smaller irradiation area and higher intensity of this irradiation method, the flakes become more fragmented as the irradiation continues, compared to the optical images shown previously. For n = 1 flakes, only the intrinsic blue PL emission was observed, and this emission gradually diminished and eventually became completely quenched under UV illumination. For n = 2 and n = 3 flakes, in addition to observing the intrinsic blue light PL emission, non-intrinsic green light PL emission was also observed. The green light PL emission was already present in freshly peeled flakes and gradually increased in intensity with longer exposure to UV light, while the blue light PL emission gradually diminished and eventually became quenched. Similar phenomena have been reported in previous literature, where 2D perovskite single crystals were irradiated with femtosecond pulse laser, causing the escape of BA molecules and the formation of 3D nanocrystals with low-energy emission.[88] Here, by scanning the samples with excitation UV light, we enabled the widespread presence of low-energy emission throughout the flakes, leading to the original lattice shrinkage from 2D to 3D structures in n = 2, 3 flakes. As a result, the blue light diminished while intense green light was emitted.

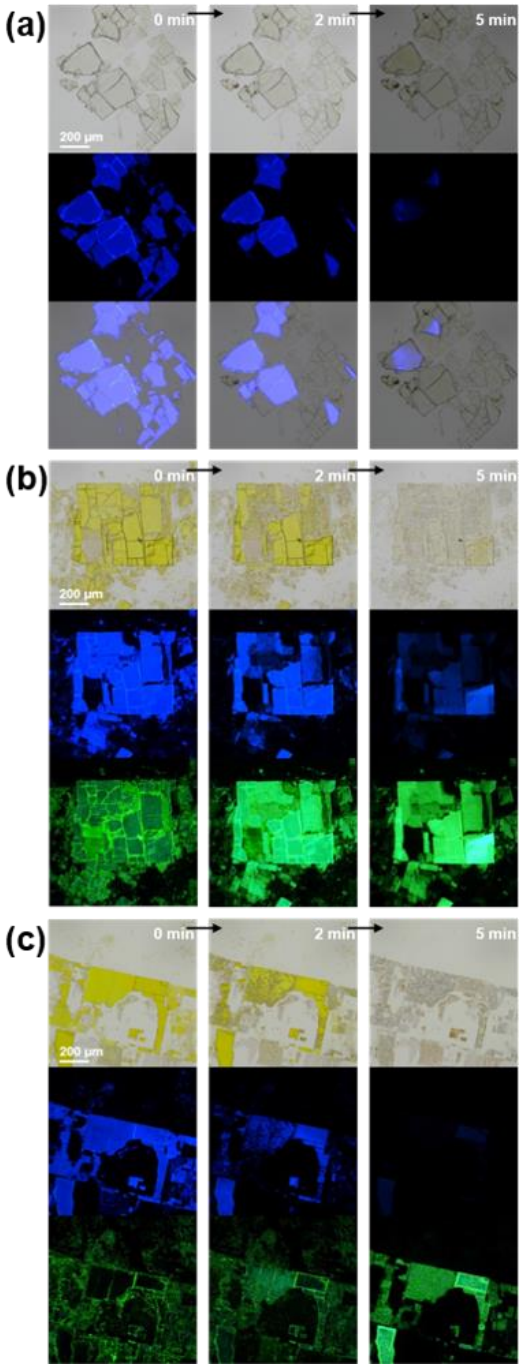

Fig. 4.6 PL imaging. (a) Top to bottom of each column: optical images, blue light emitting images and overlap of the previous two images of n = 1 flakes; (b) Top to bottom of each column: optical images, blue light emitting images, and green light emitting images of n = 2 flakes; (c) Top to bottom of each column: optical images, blue

light emitting images, and green light emitting images of n = 3 flakes.

To investigate this emission shift phenomenon induced by light illumination, we conducted a detailed PL characterization using exfoliated $(BA)_2(MA)Pb_2Br_7$ (n = 2) thin flakes as an example, as shown in **Fig. 4.7a,b**. Before exposure to UV illumination, the majority of most flakes shows a blue light emission at ~445 nm. Notably, at the same time, as shown in the PL spectra, there exists a relative week low-energy emission peak at ~525 nm emitted from few parts of the newly exfoliated flakes. This can be explained as the presence of defects generated during the process of mechanically exfoliating the flakes, leading to the random formation of low-energy states (LESs), the origin of which is disputed.[89] Similar results could also be found in exfoliated n = 3 samples while n = 1 samples show only one emission. Under continuous UV illumination, the PL emission of the flakes shifted from being predominantly blue light to being predominantly green light, as evidenced by both images and spectra. This change suggests that the intrinsic emission energy state in pristine flakes is gradually disrupted by the ultraviolet light, leading to the formation of low-energy states (LESs) during the process. Furthermore, it is worth noting that the low-energy states (LESs) tend to manifest as discrete nano-clusters rather than continuous ones. Therefore, referring to them as edge states, as mentioned in some literature, may not be entirely accurate. Extracted from the illumination-time-dependent PL emission spectrum, analysis in **Fig. 4.7c** are presented: firstly, the numerical ratio of blue light intensity to green light intensity decreases from approximately 2.5 to 0.5 (indicated by the red fitting curve, corresponding to the right axis). Secondly, the peak position of the non-intrinsic low-energy emission gradually undergoes a redshift from ~520 nm to ~530 nm

(corresponding to the left axis). The wavelength of low-energy emission is closed to PL of 3D $MAPbBr_3$ ($n = \infty$) perovskites (~535 nm). Previous literature proposed LESs to be 3D or 3D/2D heterojunction.[90] Here, we observe the gradual redshift of low-energy emission, which corresponds to the progressive growth of green nano-clusters observed in the PL images. Therefore, the reason for the emission redshift observed in $(BA)_2(MA)_{n-1}Pb_nBr_{3n+1}$ ($n > 1$) 2D perovskites under light illumination can be attributed to the light-induced formation of $MAPbBr_3$ nanoclusters.

To investigate the spatial distribution of the PL emission change induced by light illumination, we partially covered a flake with an opaque mask and subjected it to light exposure. As shown in **Fig. 4.7d**, the edge of the mask is presented by the polyline, and to the left and to the right of this line are transparent phase and mask-protected pristine bulk, respectively. Due to the effective blocking of the incident light by the mask, a two-phase interface appeared at the edges of the covered region. Across the interface of these two phases, three regions labeled as 1, 2, 3 were selected as shown in the enlarged view. A green-emitting nanocluster marked by box in the image, was selected for the analysis of its PL emission. Their PL spectrum are drawn in **Fig. 4.7e**. The PL emission of region 1 (bulk) and that of region 2 (interface) are almost the same with a dominated ~445 nm peak and a slight low-energy emission. Therefore, the possibility of non-intrinsic emission being caused by interface luminescence can essentially be ruled out. While in region 3 (transparent phase), the ~445 nm peak is totally disappeared and only remain a widespread PL peak with a center wavelength at ~520 nm. In contrast, the emission of the tiny nanocluster shows a relatively sharp peak at ~530 nm. Based on the above analysis, we can draw the following conclusions: light illumination leads to

the quenching of intrinsic blue light emission; In the transparent phase, the weak and diffuse luminescence originates from amorphous $PbBr_2$ and the combined interaction between residual small amounts of MA molecules and PbBr octahedra; the strong green light emission, on the other hand, originates from nanoclusters with a composition resembling $MAPbBr_3$.

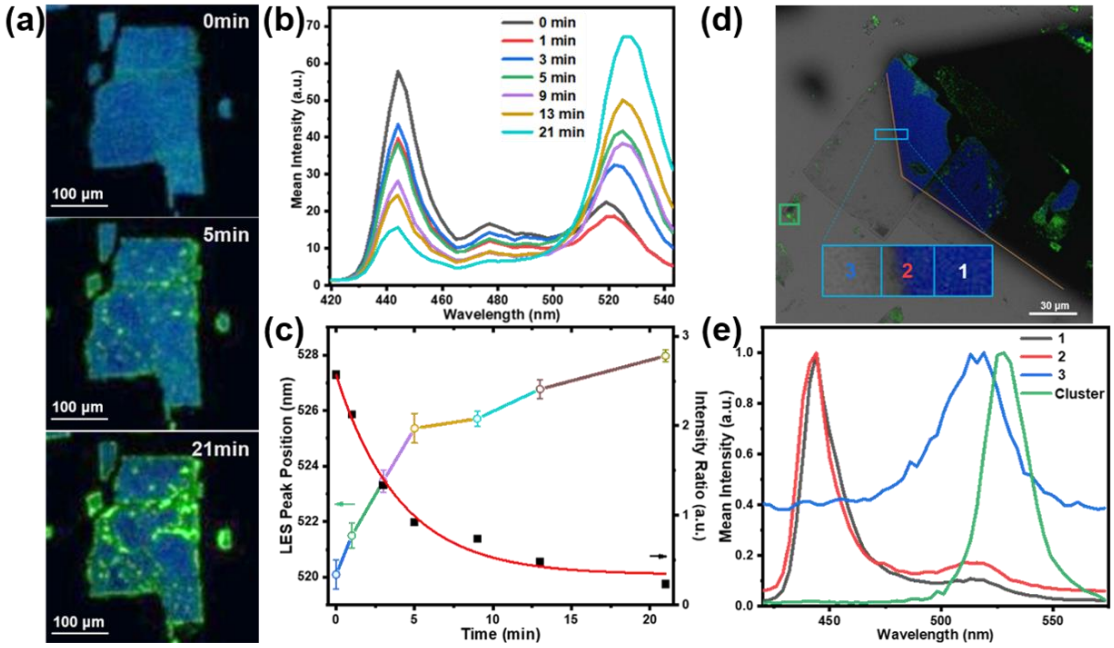

Fig. 4.7 PL characterization of n = 2. (a) PL images and (b) spectrum of exfoliated n = 2 flakes under continuous illumination, captured at different time intervals; (c) evolution of non-intrinsic low-energy emission peak position as a function of time (left axis) and intensity ratio of intrinsic emission to low-energy emission (right axis); (d) PL image of a partially covered flake and (e) spectrum of the selected regions.

A combination of TEM and SEM coupled with EDX was employed to analyze the transparent phase formed as a result of light illumination. **Fig. 4.8a** presents an optical microscope image of an n = 2 flake transferred onto a copper grid for TEM observation.

This flake has undergone UV illumination, resulting in partial degradation. The central region has transformed into a transparent phase, while the remaining parts still retain their original yellow color. The TEM image and selected area electron diffraction (SAED) patterns of this partially degraded flake is shown in **Fig. 4.8b**. The region of the transparent phase was labeled as Region I, while the remaining portion was labeled as Region II. The selected regions' SAED patterns exhibit distinct characteristics: sharp dots for Region II, indicating a relatively high crystallinity in the remaining yellow-colored part, and diffraction rings for Region I, indicating the presence of an amorphous phase as a result of light-induced degradation. Radial profiles of SAED patterns in **Fig. 4.8c** confirm that the diffraction of region II is similar to pristine n = 2 with just a little reduction of the sharpness of peaks. The diffraction rings representing the transparent phase formed through degradation exhibit a relatively broad peak, with the peak center corresponding approximately to a lattice plane spacing of 0.3 nm. By comparing the diffraction rings of degraded $(BA)_2(MA)Pb_2Br_7$ (n = 2) flakes with those of degraded $(BA)_2PbBr_4$ (n = 1) and $MAPbBr_3$ (n = ∞), it can be found that they correspond to approximately the same spacing. Based on the composition of these three samples, it is most likely that the transparent phase formed after illumination is amorphous $PbBr_2$. In addition, an SEM image and the corresponding EDX elemental analysis of a degraded n = 2 flake is show in **Fig. 4.8d**. The surface of the flakes became very rough, broken, and full of defects after exposure to UV light. The EDX analysis results obtained from sampling at three different points on this flake are listed in the table in the inserted figure, where the ratio of average atomic amount percentage of Pb and Br at these points is approximately Pb:Br ≈ 1:2. This provides further evidence of the formation of $PbBr_2$

after illumination.

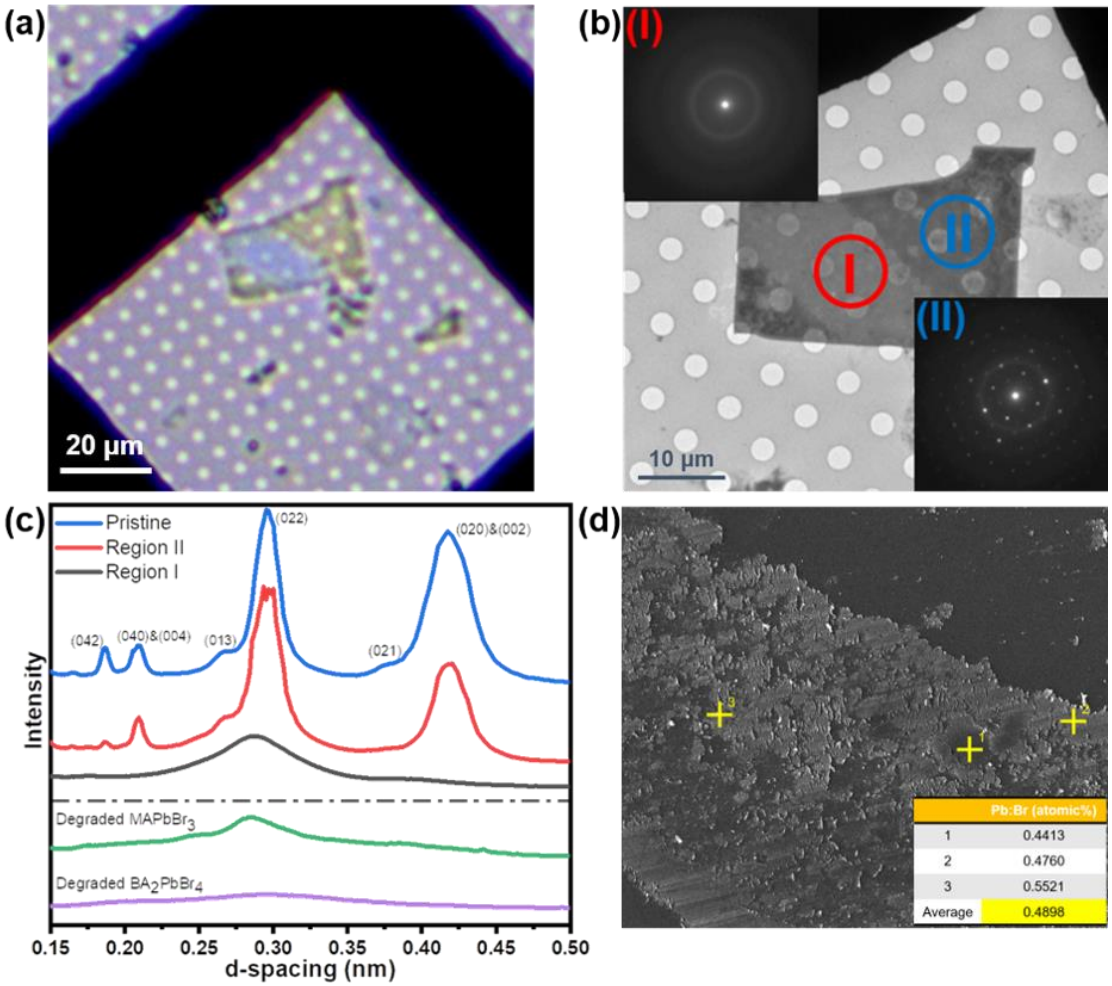

Fig. 4.8 TEM and SEM characterization. (a) Optical and (b) TEM image of an n = 2 flake after illumination (inserted are SAED of selected regions); (c) radial average peak fitting of SAED for different region on the n = 2 flake and other samples; (d) SEM image of a degraded n = 2 flake and EDX data extracted at three points.

To monitor the morphological changes under UV illumination, AFM was applied to measure the surface morphology and thickness variation of exfoliated $(BA)_2(MA)Pb_2Br_7$ (n = 2) thin flakes. In **Fig. 4.9a**, AFM images of an n = 2 flake are shown, where

the same flake were measured before and after 30 min of UV illumination, respectively. The corresponding height profiles (**Fig. 4.9b**) obtained along the dotted lines suggests that after illumination, the surface of the flake become rough with roughness increases from about 0.85 nm to 4.5 nm, and its average thickness reduce from 48 nm to 29 nm. Despite the potential impact of the laser used during the AFM testing process, the freshly exfoliated flakes exhibit highly smooth surfaces. After a 30-minute exposure to illumination, surface defects emerged, leading to a significant increase in surface roughness. It is intriguing to observe that the thin flake exhibits a reduction in thickness to approximately 40% of its original thickness. In a unit cell of n = 2 crystal structure, the length along the c-axis of the long chain layer consist of BA organic molecules accounts for about 40% of the length along the direction of the whole unit cell. This correspondence has important implications for revealing that the organic layers are removed under exposure to UV illumination, while the octahedral $PbBr_6$ layers are preserved and continue to exist as Pb-Br compounds. It is the organic interlayers degrade under UV illumination and lead to the collapse of the crystal structure.

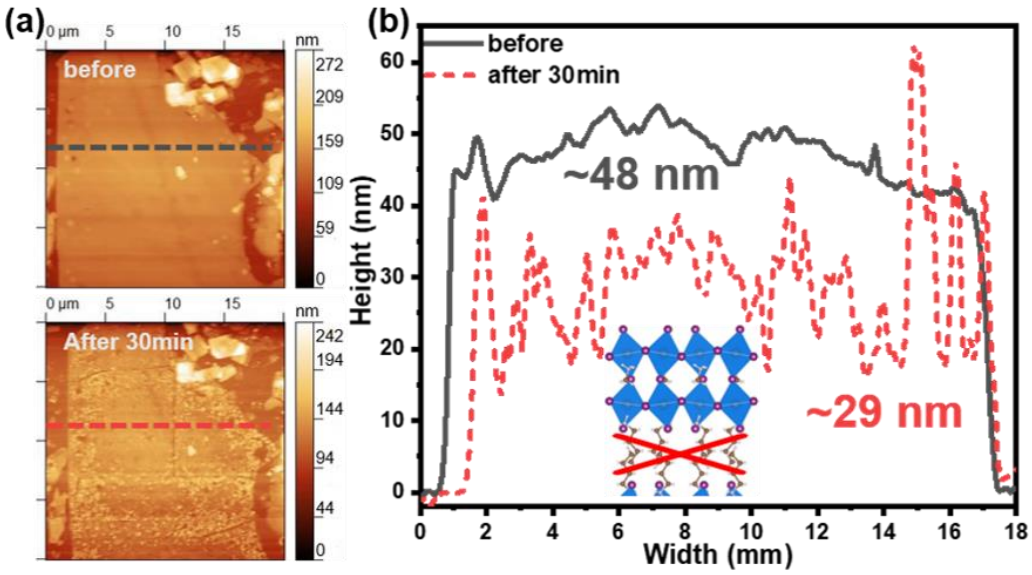

Fig. 4.9 AFM characterization of a thin n = 2 flake under illumination for 30 min. (a) AFM images and (b) sample height profile of the flake before and after illumination.

The experiments demonstrate that thicker flakes exhibit better tolerance to UV light illumination. **Fig. 4.10** illustrates the thickness variation of a thick n = 3 flake (~300 nm) after undergoing 60 minutes of UV light illumination. After such a prolonged duration of light exposure, the thickness of the flake only decreased by approximately 20%, which is significantly less than the extent of thickness reduction observed in thinner flakes. This can be explained by the fact that, as UV irradiation causes degradation in the few outermost layers of the lattice closer to the light source, the remaining amorphous $PbBr_2$ impedes further penetration of UV light, thereby protecting the inner layers of the lattice and effectively slowing down light-induced degradation.

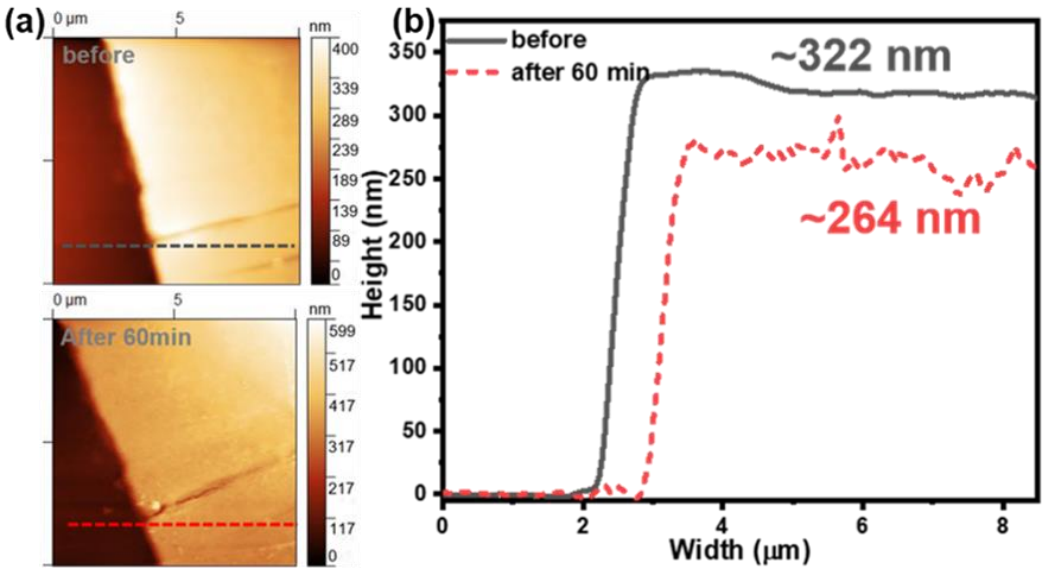

Fig. 4.10 AFM characterization of a thick n = 3 flake under illumination for 60 min. (a) AFM images and (b) sample height profile of the flake before and after illumination.

FTIR technique can detect the absence of BA and even the alteration in the BA to MA ratio[60, 91, 92] and has been applied to study the $(BA)_2(MA)_{n-1}Pb_nBr_{3n+1}$ perovskites in previous literature[90]. The peak at ~1480 cm^{-1} corresponds to methyl group ($-CH_3$) vibration and peak at ~1580 cm^{-1} corresponds to amine group ($-NH_3$) vibration. Although both BA and MA molecules contain these two groups, the change in the ratio of BA to MA can be confirmed by comparing the relative intensity of peak located at ~1480 and 1580 cm^{-1}. As shown in **Fig. 4.12a**, according to the comparison of the intensity of two peaks, $(BA)_2(MA)_{n-1}Pb_nBr_{3n+1}$ materials with different value of n (1, 2, 3, ∞) can be distinguished. **Fig. 4.12b,c,d** show the evolution of FTIR spectrum of exfoliated flakes under continuous illumination. The peak intensity of~1480 to 1580 cm^{-1} both reduce over time, which suggests that organic molecules MA and BA both decompose under UV illumination. Followed by analysis of the two feature peaks in spectrum of n = 2 (**Fig. 4.12e,f**), the peak intensity ratio of ~1480 to 1580 cm^{-1} remain almost unchanged. These results implicate that, from an overall perspective, both BA and MA organic molecules decompose, and statistically there is no case that MA molecules are protected by the octahedral layer and decompose at a slower rate than BA organic interlayer.

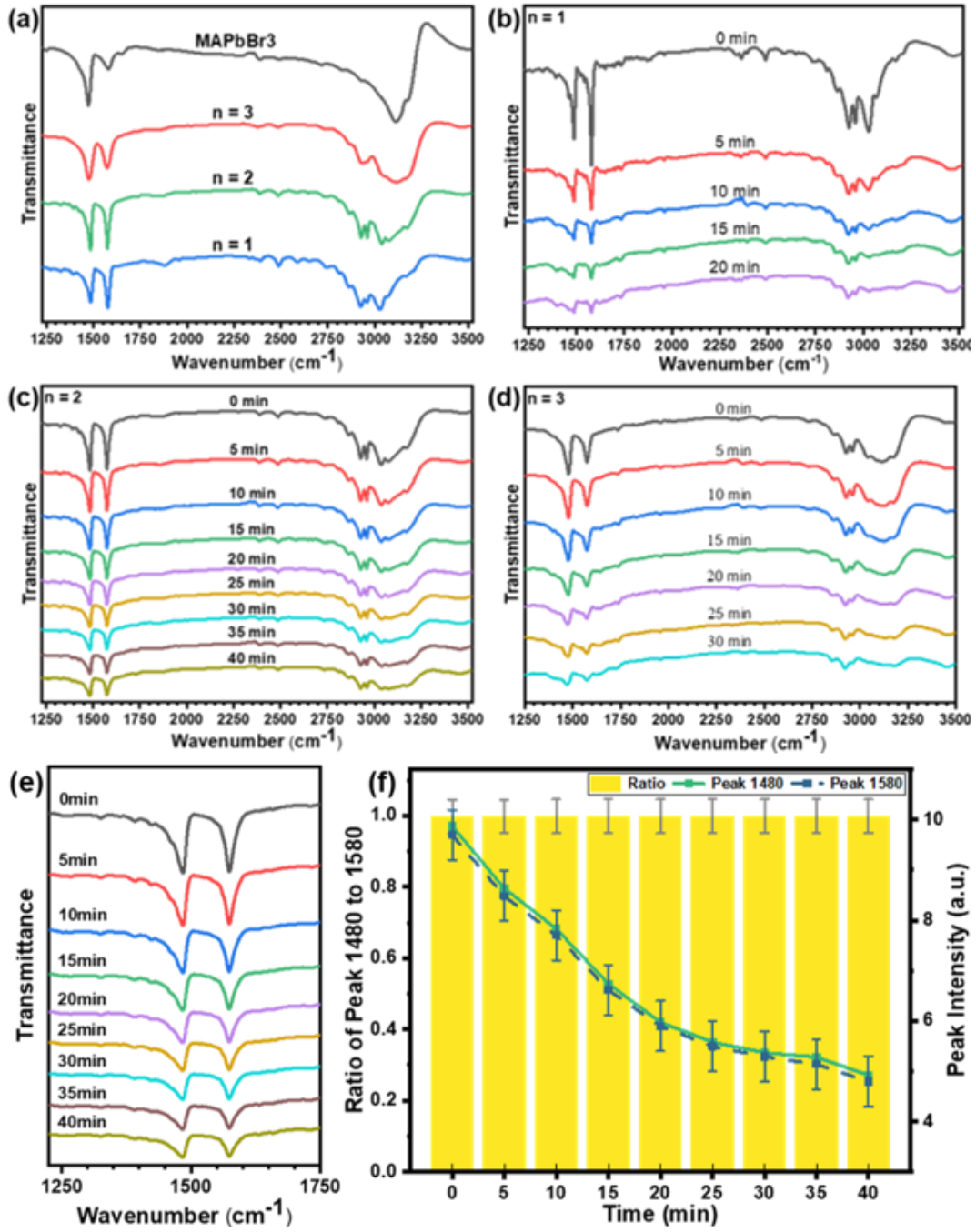

Fig. 4.11 Quasi-in-situ FTIR spectrum of perovskites. (a) FTIR spectrum of $(BA)_2(MA)_{n-1}Pb_nBr_{3n+1}$ (n = 1, 2, 3, ∞) perovskites; (b) evolution of FTIR spectrum of n = 1 under continuous illumination; (c) evolution of FTIR spectrum of n = 2 under continuous illumination; (d) evolution of FTIR spectrum of n = 3 under continuous

illumination. (e) FTIR spectrum plot of n = 2 with a wavenumber range of 1250 to 1750 cm^{-1}, and (f) intensity change of the two featured peaks and their ratio.

The frequencies of hydrogen vibrations in CH_3 (MA^+) and CH_3 (BA^+) were calculated to be approximately 1470 and 1482 cm^{-1}, respectively.[90] In **Fig. 4.12**, we compare the escape velocities of BA and MA molecules under light illumination by analyzing the featured peak at ~1480 cm^{-1}. The two prominent sub-peaks separated from the ~1480 cm^{-1} peak, represented by the red and blue curves in the figure, correspond respectively to MA and BA. Using these two sub-peaks as a measure of the organic molecule content, and considering their intensities as a function of light exposure time, we found that BA is more significantly affected by light illumination and exhibits a faster escape velocity compared to MA. This can be explained by the fact that BA molecules are distributed as intercalants between octahedral layers, while MA molecules are surrounded by inorganic octahedra, making them less prone to escape. After approximately 30 minutes of light exposure, the variation in the content of MA and BA enters a plateau, which may be attributed to the depletion of most organic molecules on the sample surface, while the relatively deeper organic molecules are less likely to escape.

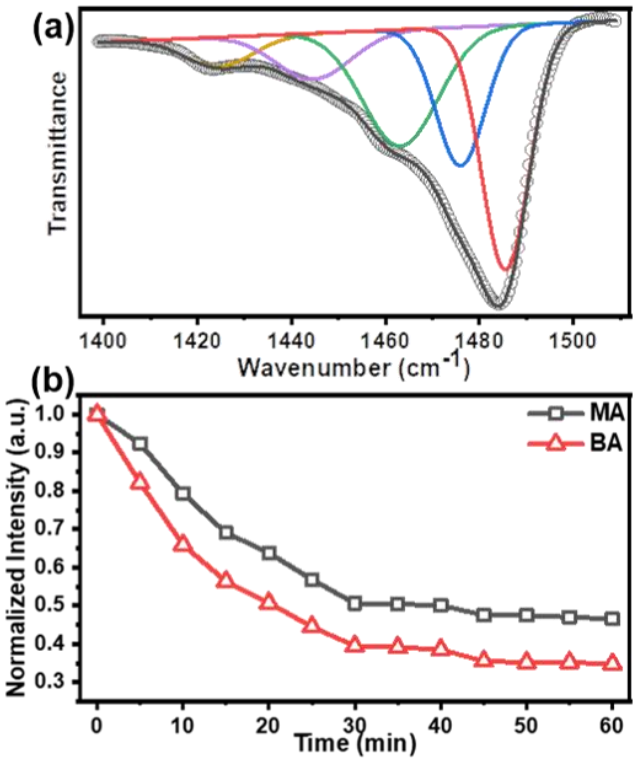

Fig. 4.12 Peak analysis of ~1480 cm^{-1} featured peak in FTIR spectrum of n = 2. (a) Peak fitting of the ~1480 cm^{-1} peak, where the red peak is considered to correspond to the major hydrogen vibrations in MA, and the blue peak is attributed to the major hydrogen vibrations in BA; (b) the intensity of the peaks corresponding to the two organic molecules varies with the illumination time.

The schematic in **Fig. 4.13** illustrates the UV light-induced changes on 2D perovskites and underlying mechanism, as proposed based on our comprehensive analysis of all the experimental results mentioned above. Under the illumiation of UV light, organic molecules begin to escape from the lattice, with the intercalated BA molecules being more prone to escape compared to the MA molecules within the octahedral layers. In the majority of the exposed regions, the loss of organic molecules leads to lattice collapse, leaving behind amorphous $PbBr_2$, which corresponds to the

transparent phase observed in our experiments. However, at certain edges or defects, the slower escape rate of MA molecules results in the formation of quasi-$MAPbBr_3$ nanoclusters with surrounding $[PbBr_6]^{4-}$ octahedra, emitting intense green light that replaces the intrinsic PL emission. This is the underlying mechanism behind the emission and structural transformation induced by UV light.

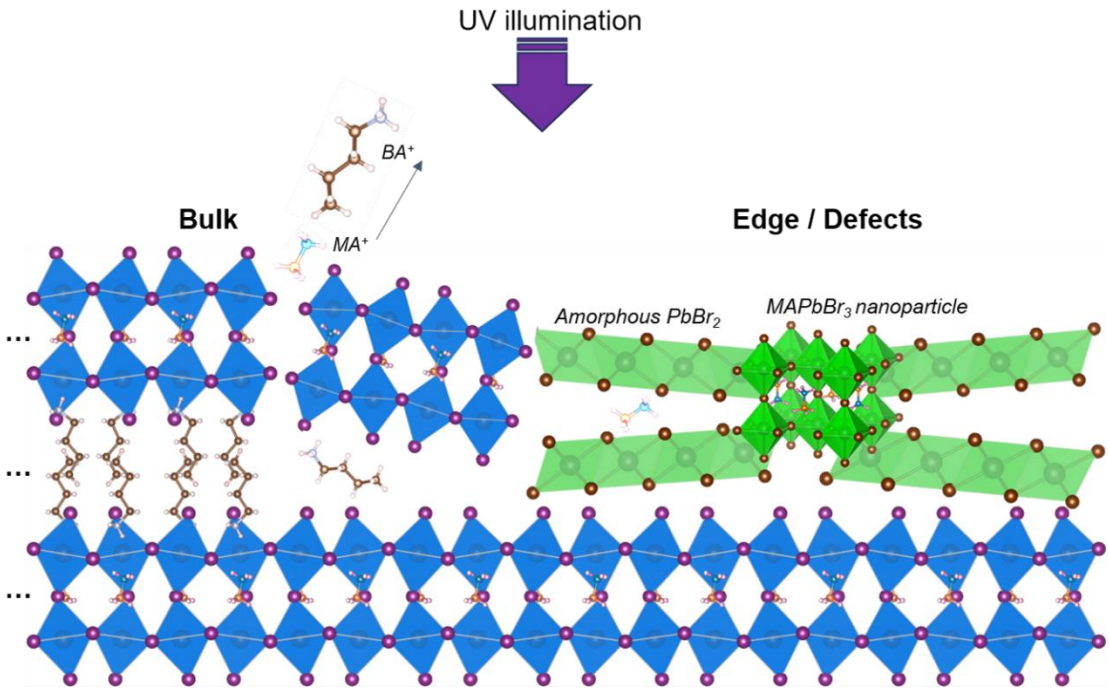

Fig. 4.13 Schematic of UV illumination-induced degradation and formation of 3D nanoparticles.

4.4 Summary

In summary, we studied the emission redshift and degradation of $(BA)_2(MA)_{n-1}Pb_nBr_{3n+1}$ 2D perovskites under UV light illumination. By exposing the exfoliated flakes to UV light, the crystalline structure of $(BA)_2(MA)_{n-1}Pb_nBr_{3n+1}$ collapses and transformed into amorphous $PbBr_2$ due to light-induced loss of organic

components. Notably, we found that the PL performance of $n > 2$ exhibit a redshift from blue to green. This emission transformation can be attributed to the degradation of pristine crystal and randomly formed $MAPbBr_3$ nanoclusters produced during the illumination process with the existence of MA^+ and $[PbBr_6]^{4-}$ octahedra. These results are important for understanding the PL emission transition and degradation mechanism of these perovskites and paves the way for the design of photostable optoelectronic applications.

Chapter 5 Conclusions and Future Prospect

5.1 Conclusions

In recent years, 2D perovskites have gained significant attention due to their improved humidity stability compared to 3D counterparts; however, research on the light-induced degradation of 2D perovskites remains under debate, while their PL emission behavior remains an intriguing phenomenon. This study was an attempt to investigate the response of layered perovskites under UV light illumination, particularly focusing on the light-induced degradation and redshifted emission, while providing an explanation for the underlying mechanisms. In this experiment, we employed quasi in-situ characterization techniques to observe the changes in 2D perovskite nanoflakes under illumination. By analyzing multiple characterization results, we outlined a comprehensive picture of the response of 2D perovskites to UV light. Due to the light-induced loss of organic components, the crystalline structure of $(BA)_2(MA)_{n-1}Pb_nBr_{3n+1}$ undergoes collapse, leaving behind amorphous $PbBr_2$. The redshift of PL observed in samples with $n > 1$ can be attributed to the formation of $MAPbBr_3$ nanoclusters, which easily form at defect sites due to the slower escape velocity of MA molecules and their subsequent association with $[PbBr_6]^{4-}$ octahedra. The implications of the results are clear for understanding of light-induced emission and structural transformations in 2D perovskites. This research has the potential to pave the way for the development of novel strategies and materials that can enhance the stability and performance of optoelectronic devices in the presence of light.

5.2 Future Prospect

Based on the findings of the current study, Additional work could be done on:

(1) Explore the impact of other environmental factors, such as oxygen, moisture, and temperature, and investigate their effects on the stability of the material under consideration, taking into account the potential external stimuli that the material may encounter in practical applications.

(2) Design and optimize encapsulation methods to protect layered perovskite crystals from light-induced degradation. Explore various encapsulation materials or coatings to minimize the effects of different external factors on the crystal structure.

(3) Evaluating the long-term stability and efficiency of 2D perovskite-based devices under various operating conditions. To achieve this, there is a need to develop more advanced characterization techniques that enable real-time monitoring and analysis of the degradation processes.

References

(1) A. Kojima, K. Teshima, Y. Shirai, and T. Miyasaka, "Organometal Halide Perovskites as Visible-Light Sensitizers for Photovoltaic Cells," *Journal of the American Chemical Society,* vol. 131, no. 17, pp. 6050-+, May 2009.

(2) S. De Wolf *et al.*, "Organometallic Halide Perovskites: Sharp Optical Absorption Edge and Its Relation to Photovoltaic Performance," *Journal of Physical Chemistry Letters,* vol. 5, no. 6, pp. 1035-1039, Mar 2014.

(3) H. Oga, A. Saeki, Y. Ogomi, S. Hayase, and S. Seki, "Improved Understanding of the Electronic and Energetic Landscapes of Perovskite Solar Cells: High Local Charge Carrier Mobility, Reduced Recombination, and Extremely Shallow Traps," *Journal of the American Chemical Society,* vol. 136, no. 39, pp. 13818-13825, Oct 2014.

(4) S. D. Stranks *et al.*, "Electron-Hole Diffusion Lengths Exceeding 1 Micrometer in an Organometal Trihalide Perovskite Absorber," vol. 342, no. 6156, pp. 341-344, 2013.

(5) J. M. Frost, K. T. Butler, F. Brivio, C. H. Hendon, M. van Schilfgaarde, and A. Walsh, "Atomistic Origins of High-Performance in Hybrid Halide Perovskite Solar Cells," *Nano Letters,* vol. 14, no. 5, pp. 2584-2590, 2014/05/14 2014.

(6) A. K. Jena, A. Kulkarni, and T. Miyasaka, "Halide Perovskite Photovoltaics: Background, Status, and Future Prospects," *Chemical Reviews,* vol. 119, no. 5, pp.

3036-3103, Mar 2019.

(7) S. A. Veldhuis *et al.*, "Perovskite Materials for Light-Emitting Diodes and Lasers," *Advanced Materials,* vol. 28, no. 32, pp. 6804-6834, Aug 2016.

(8) H. Wang and D. H. Kim, "Perovskite-based photodetectors: materials and devices," *Chemical Society Reviews,* vol. 46, no. 17, pp. 5204-5236, Sep 2017.

(9) F. De Angelis, "Celebrating 10 Years of Perovskite Photovoltaics," *ACS Energy Letters,* vol. 4, no. 4, pp. 853-854, 2019/04/12 2019.

(10) L. B. Fan, Z. F. Pei, P. Wang, and Z. Zheng, "Research Progress on the Stability of Organic-Inorganic Halide Perovskite Photodetectors in a Humid Environment Through the Modification of Perovskite Layers," *Journal of Electronic Materials,* vol. 51, no. 6, pp. 2801-2818, Jun 2022.

(11) T. T. Xu, L. X. Chen, Z. H. Guo, and T. L. Ma, "Strategic improvement of the long-term stability of perovskite materials and perovskite solar cells," *Physical Chemistry Chemical Physics,* vol. 18, no. 39, pp. 27026-27050, Oct 2016.

(12) J. L. Yang and T. L. Kelly, "Decomposition and Cell Failure Mechanisms in Lead Halide Perovskite Solar Cells," *Inorganic Chemistry,* vol. 56, no. 1, pp. 92-101, Jan 2017.

(13) J. B. Huang, S. Q. Tan, P. D. Lund, and H. P. Zhou, "Impact of H2O on organic-inorganic hybrid perovskite solar cells," *Energy & Environmental Science,* vol. 10, no. 11, pp. 2284-2311, Nov 2017.

(14) Q. Lu *et al.*, "A Review on Encapsulation Technology from Organic Light Emitting Diodes to Organic and Perovskite Solar Cells," *Advanced Functional Materials,* vol. 31, no. 23, Jun 2021, Art. no. 2100151.

(15) J. L. Li *et al.*, "Encapsulation of perovskite solar cells for enhanced stability: Structures, materials and characterization," *Journal of Power Sources,* vol. 485, Feb 2021, Art. no. 229313.

(16) S. Z. Butler *et al.*, "Progress, Challenges, and Opportunities in Two-Dimensional Materials Beyond Graphene," *ACS Nano,* vol. 7, no. 4, pp. 2898-2926, 2013/04/23 2013.

(17) L. Mao, C. C. Stoumpos, and M. G. Kanatzidis, "Two-Dimensional Hybrid Halide Perovskites: Principles and Promises," *Journal of the American Chemical Society,* vol. 141, no. 3, pp. 1171-1190, 2019/01/23 2019.

(18) T. M. Koh, B. Febriansyah, and N. Mathews, "Ruddlesden-Popper Perovskite Solar Cells," *Chem,* vol. 2, no. 3, pp. 326-327, Mar 2017.

(19) D. H. Cao, C. C. Stoumpos, O. K. Farha, J. T. Hupp, and M. G. Kanatzidis, "2D Homologous Perovskites as Light-Absorbing Materials for Solar Cell Applications," *Journal of the American Chemical Society,* vol. 137, no. 24, pp. 7843-7850, Jun 2015.

(20) H. Lin *et al.*, "Single-phase alkylammonium cesium lead iodide quasi-2D perovskites for color-tunable and spectrum-stable red LEDs," *Nanoscale,* vol. 11, no. 36, pp. 16907-16918, Sep 2019.

(21) Y. Zhu, X. Q. Sun, Y. L. Tang, L. Fu, and Y. R. Lu, "Two-dimensional materials for light emitting applications: Achievement, challenge and future perspectives," *Nano Research,* vol. 14, no. 6, pp. 1912-1936, Jun 2021.

(22) F. J. Liu *et al.*, "2D Ruddlesden-Popper Perovskite Single Crystal Field-Effect Transistors," *Advanced Functional Materials,* vol. 31, no. 1, Jan 2021, Art. no. 2005662.

(23) M. Gedda *et al.*, "Ruddlesden-Popper-Phase Hybrid Halide Perovskite/Small-Molecule Organic Blend Memory Transistors," *Advanced Materials,* vol. 33, no. 7, Feb 2021, Art. no. 2003137.

(24) J. C. Zhou, Y. L. Chu, and J. Huang, "Photodetectors Based on Two-Dimensional Layer-Structured Hybrid Lead Iodide Perovskite Semiconductors," *Acs Applied Materials & Interfaces,* vol. 8, no. 39, pp. 25660-25666, Oct 2016.

(25) L. L. Min, W. Tian, F. R. Cao, J. Guo, and L. Li, "2D Ruddlesden-Popper Perovskite with Ordered Phase Distribution for High-Performance Self-Powered Photodetectors," *Advanced Materials,* vol. 33, no. 35, Sep 2021, Art. no. 2101714.

(26) H. H. Fang *et al.*, "Unravelling Light-Induced Degradation of Layered Perovskite Crystals and Design of Efficient Encapsulation for Improved Photostability," *Advanced Functional Materials,* vol. 28, no. 21, May 2018, Art. no. 1800305.

(27) L. F. Nie, X. X. Ke, and M. L. Sui, "Microstructural Study of Two-Dimensional Organic-Inorganic Hybrid Perovskite Nanosheet Degradation under Illumination," *Nanomaterials,* vol. 9, no. 5, May 2019, Art. no. 722.

(28) M. Seitz, P. Gant, A. Castellanos-Gomez, and F. Prins, "Long-Term Stabilization of Two-Dimensional Perovskites by Encapsulation with Hexagonal Boron Nitride," *Nanomaterials,* vol. 9, no. 8, Aug 2019, Art. no. 1120.

(29) A. Coriolano *et al.*, "Improved Photostability in Fluorinated 2D Perovskite Single Crystals," *Nanomaterials,* vol. 11, no. 2, Feb 2021, Art. no. 465.

(30) D. Weber, "CH3NH3PbX3, ein Pb(II)-System mit kubischer Perowskitstruktur / CH3NH3PbX3, a Pb(II)-System with Cubic Perovskite Structure," vol. 33, no. 12, pp. 1443-1445, 1978.

(31) B. Saparov and D. B. Mitzi, "Organic–Inorganic Perovskites: Structural Versatility for Functional Materials Design," *Chemical Reviews,* vol. 116, no. 7, pp. 4558-4596, 2016/04/13 2016.

(32) V. M. Goldschmidt, "Die Gesetze der Krystallochemie," *Naturwissenschaften,* vol. 14, no. 21, pp. 477-485, 1926/05/01 1926.

(33) X. X. Tian, Y. Z. Zhang, R. K. Zheng, D. Wei, and J. Q. Liu, "Two-dimensional organic-inorganic hybrid Ruddlesden-Popper perovskite materials: preparation, enhanced stability, and applications in photodetection," *Sustainable Energy & Fuels,* vol. 4, no. 5, pp. 2087-2113, May 2020.

(34) H.-S. Kim *et al.*, "Lead Iodide Perovskite Sensitized All-Solid-State Submicron Thin Film Mesoscopic Solar Cell with Efficiency Exceeding 9%," *Scientific Reports,* vol. 2, no. 1, p. 591, 2012/08/21 2012.

(35) G. C. Xing *et al.*, "Low-temperature solution-processed wavelength-tunable perovskites for lasing," *Nature Materials,* vol. 13, no. 5, pp. 476-480, May 2014.

(36) F. Li *et al.*, "Ambipolar solution-processed hybrid perovskite phototransistors," *Nature Communications,* vol. 6, Sep 2015, Art. no. 8238.

(37) Y. Zhang *et al.*, "Ultrasensitive Photodetectors Based on Island-Structured CH3NH3PbI3 Thin Films," *ACS Applied Materials & Interfaces,* vol. 7, no. 39, pp. 21634-21638, 2015/10/07 2015.

(38) H. Kim, J. S. Han, J. Choi, S. Y. Kim, and H. W. Jang, "Halide Perovskites for Applications beyond Photovoltaics," *Small Methods,* vol. 2, no. 3, Mar 2018, Art. no. 1700310.

(39) E. Aktas *et al.*, "Challenges and strategies toward long-term stability of lead-free tin-based perovskite solar cells," *Communications Materials,* vol. 3, no. 1, p. 104, 2022/12/23 2022.

(40) M. A. Afroz *et al.*, "Design potential and future prospects of lead-free halide perovskites in photovoltaic devices," *Journal of Materials Chemistry A,* 10.1039/D2TA07687J vol. 11, no. 25, pp. 13133-13173, 2023.

(41) N. Aristidou *et al.*, "The Role of Oxygen in the Degradation of Methylammonium Lead Trihalide Perovskite Photoactive Layers," *Angewandte Chemie-International Edition,* vol. 54, no. 28, pp. 8208-8212, 2015.

(42) H. H. Fang *et al.*, "Ultrahigh sensitivity of methylammonium lead tribromide

perovskite single crystals to environmental gases," *Science Advances,* vol. 2, no. 7, Jul 2016, Art. no. e1600534.

(43) A. Zohar *et al.*, "Impedance Spectroscopic Indication for Solid State Electrochemical Reaction in (CH3NH3)Pbl(3) Films," *Journal of Physical Chemistry Letters,* vol. 7, no. 1, pp. 191-197, Jan 2016.

(44) W. G. Kong, A. Rahimi-Iman, G. Bi, X. S. Dai, and H. Z. Wu, "Oxygen Intercalation Induced by Photocatalysis on the Surface of Hybrid Lead Halide Perovskites," *Journal of Physical Chemistry C,* vol. 120, no. 14, pp. 7606-7611, Apr 2016.

(45) Y. Q. Luo *et al.*, "Direct Observation of Halide Migration and its Effect on the Photoluminescence of Methylammonium Lead Bromide Perovskite Single Crystals," *Advanced Materials,* vol. 29, no. 43, Nov 2017, Art. no. 1703451.

(46) W. Nie *et al.*, "Light-activated photocurrent degradation and self-healing in perovskite solar cells," *Nature Communications,* vol. 7, May 2016, Art. no. 11574.

(47) C. G. Bischak *et al.*, "Origin of Reversible Photoinduced Phase Separation in Hybrid Perovskites," *Nano Letters,* vol. 17, no. 2, pp. 1028-1033, Feb 2017.

(48) D. J. Slotcavage, H. I. Karunadasa, and M. D. McGehee, "Light-Induced Phase Segregation in Halide-Perovskite Absorbers," *Acs Energy Letters,* vol. 1, no. 6, pp. 1199-1205, Dec 2016.

(49) E. T. Hoke, D. J. Slotcavage, E. R. Dohner, A. R. Bowring, H. I. Karunadasa, and

M. D. McGehee, "Reversible photo-induced trap formation in mixed-halide hybrid perovskites for photovoltaics," *Chemical Science,* vol. 6, no. 1, pp. 613-617, 2015.

(50) Y. H. Seo, J. H. Kim, D. H. Kim, H. S. Chung, and S. I. Na, "In situ TEM observation of the heat-induced degradation of single- and triple-cation planar perovskite solar cells," *Nano Energy,* vol. 77, Nov 2020, Art. no. 105164.

(51) P. P. Mohanty, R. Ahuja, and S. Chakraborty, "Progress and challenges in layered two-dimensional hybrid perovskites," *Nanotechnology,* vol. 33, no. 29, Jul 2022, Art. no. 292501.

(52) L. L. Mao, C. C. Stoumpos, and M. G. Kanatzidis, "Two-Dimensional Hybrid Halide Perovskites: Principles and Promises," *Journal of the American Chemical Society,* vol. 141, no. 3, pp. 1171-1190, Jan 2019.

(53) K. Leng, W. Fu, Y. P. Liu, M. Chhowalla, and K. P. Loh, "From bulk to molecularly thin hybrid perovskites," *Nature Reviews Materials,* vol. 5, no. 7, pp. 482-500, Jul 2020.

(54) Z. J. Tan *et al.*, "Two-Dimensional (C4H9NH3)(2)PbBr4 Perovskite Crystals for High-Performance Photodetector," *Journal of the American Chemical Society,* vol. 138, no. 51, pp. 16612-16615, Dec 2016.

(55) I. C. Smith, E. T. Hoke, D. Solis-Ibarra, M. D. McGehee, and H. I. Karunadasa, "A Layered Hybrid Perovskite Solar-Cell Absorber with Enhanced Moisture Stability," *Angewandte Chemie-International Edition,* vol. 53, no. 42, pp. 11232-11235, Oct 2014.

(56) H. Tsai *et al.*, "Stable Light-Emitting Diodes Using Phase-Pure Ruddlesden-Popper Layered Perovskites," *Advanced Materials,* vol. 30, no. 6, Feb 2018, Art. no. 1704217.

(57) T. L. Leung, I. Ahmad, A. A. Syed, A. M. C. Ng, J. Popović, and A. B. Djurišić, "Stability of 2D and quasi-2D perovskite materials and devices," *Communications Materials,* vol. 3, no. 1, p. 63, 2022/09/06 2022.

(58) M. D. Smith, B. A. Connor, and H. I. Karunadasa, "Tuning the Luminescence of Layered Halide Perovskites," *Chemical Reviews,* vol. 119, no. 5, pp. 3104-3139, Mar 2019.

(59) M. L. Liang *et al.*, "Free Carriers versus Self-Trapped Excitons at Different Facets of Ruddlesden-Popper Two-Dimensional Lead Halide Perovskite Single Crystals," *Journal of Physical Chemistry Letters,* vol. 12, no. 20, pp. 4965-4971, May 2021.

(60) C. C. Stoumpos *et al.*, "Ruddlesden-Popper Hybrid Lead Iodide Perovskite 2D Homologous Semiconductors," *Chemistry of Materials,* vol. 28, no. 8, pp. 2852-2867, Apr 2016.

(61) Y. Gao *et al.*, "Molecular engineering of organic-inorganic hybrid perovskites quantum wells," *Nature Chemistry,* vol. 11, no. 12, pp. 1151-1157, Dec 2019.

(62) L. Li *et al.*, "Two-Step Growth of 2D Organic-Inorganic Perovskite Microplates and Arrays for Functional Optoelectronics," *Journal of Physical Chemistry Letters,* vol. 9, no. 16, pp. 4532-4538, Aug 2018.

(63) X. X. He *et al.*, "Oriented Growth of Ultrathin Single Crystals of 2D Ruddlesden-Popper Hybrid Lead Iodide Perovskites for High-Performance Photodetectors," *Acs Applied Materials & Interfaces,* vol. 11, no. 17, pp. 15905-15912, May 2019.

(64) Y. N. Chen *et al.*, "Tailoring Organic Cation of 2D Air-Stable Organometal Halide Perovskites for Highly Efficient Planar Solar Cells," *Advanced Energy Materials,* vol. 7, no. 18, Sep 2017, Art. no. 1700162.

(65) Y. J. Hofstetter, I. Garcia-Benito, F. Paulus, S. Orlandi, G. Grancini, and Y. Vaynzof, "Vacuum-Induced Degradation of 2D Perovskites," *Frontiers in Chemistry,* vol. 8, Feb 2020, Art. no. 66.

(66) A. A. Sutanto *et al.*, "In Situ Analysis Reveals the Role of 2D Perovskite in Preventing Thermal-Induced Degradation in 2D/3D Perovskite Interfaces," *Nano Letters,* vol. 20, no. 5, pp. 3992-3998, May 2020.

(67) F. Fiorentino, M. D. Albaqami, I. Poli, and A. Petrozza, "Thermal- and Light-Induced Evolution of the 2D/3D Interface in Lead-Halide Perovskite Films," *ACS Applied Materials & Interfaces,* vol. 14, no. 30, pp. 34180-34188, 2022/08/03 2022.

(68) H. J. Jung, C. C. Stompus, M. G. Kanatzidis, and V. P. Dravid, "Self-Passivation of 2D Ruddlesden-Popper Perovskite by Polytypic Surface PbI2 Encapsulation," *Nano Letters,* vol. 19, no. 9, pp. 6109-6117, Sep 2019.

(69) Y. Wei, P. Audebert, L. Galmiche, J. S. Lauret, and E. Deleporte, "Photostability of 2D Organic-Inorganic Hybrid Perovskites," *Materials,* vol. 7, no. 6, pp. 4789-

4802, Jun 2014.

(70) Z. Zeng *et al.*, "Photo-Induced Degradation of 2D Dion−Jacobson Perovskites under Continuous Light Illumination," *Solar Rrl,* vol. 6, no. 10, p. 2200359, 2022.

(71) N. N. Udalova *et al.*, "Nonmonotonic Photostability of BA(2)MA(n-1)Pb(n)I(3n+1) Homologous Layered Perovskites," *Acs Applied Materials & Interfaces,* vol. 14, no. 1, pp. 961-970, Jan 2022.

(72) K. S. Novoselov *et al.*, "Two-dimensional atomic crystals," vol. 102, no. 30, pp. 10451-10453, 2005.

(73) W. Niu, A. Eiden, G. V. Prakash, and J. J. Baumberg, "Exfoliation of self-assembled 2D organic-inorganic perovskite semiconductors," *Applied Physics Letters,* vol. 104, no. 17, Apr 2014, Art. no. 171111.

(74) O. Yaffe *et al.*, "Excitons in ultrathin organic-inorganic perovskite crystals," *Physical Review B,* vol. 92, no. 4, Jul 2015, Art. no. 045414.

(75) J. Z. Li *et al.*, "Fabrication of single phase 2D homologous perovskite microplates by mechanical exfoliation," *2d Materials,* vol. 5, no. 2, Apr 2018, Art. no. 021001.

(76) Z. Guo, X. X. Wu, T. Zhu, X. Y. Zhu, and L. B. Huang, "Electron-Phonon Scattering in Atomically Thin 2D Perovskites," *Acs Nano,* vol. 10, no. 11, pp. 9992-9998, Nov 2016.

(77) S. T. Ha, C. Shen, J. Zhang, and Q. H. Xiong, "Laser cooling of organic-inorganic lead halide perovskites," *Nature Photonics,* vol. 10, no. 2, pp. 115-+, Feb 2016.

(78) L. F. Zhao, H. Tian, S. H. Silver, A. Kahn, T. L. Ren, and B. P. Rand, "Ultrasensitive Heterojunctions of Graphene and 2D Perovskites Reveal Spontaneous Iodide Loss," *Joule,* vol. 2, no. 10, pp. 2133-2144, Oct 2018.

(79) V. A. Hintermayr *et al.*, "Tuning the Optical Properties of Perovskite Nanoplatelets through Composition and Thickness by Ligand-Assisted Exfoliation," *Advanced Materials,* vol. 28, no. 43, pp. 9478-+, Nov 2016.

(80) D. B. Williams and C. B. Carter, "The Transmission Electron Microscope," in *Transmission Electron Microscopy: A Textbook for Materials Science*, D. B. Williams and C. B. Carter, Eds. Boston, MA: Springer US, 2009, pp. 3-22.

(81) Z. Z. Chen, Y. W. Guo, E. Wertz, and J. Shi, "Merits and Challenges of Ruddlesden-Popper Soft Halide Perovskites in Electro-Optics and Optoelectronics," *Advanced Materials,* vol. 31, no. 1, Jan 2019, Art. no. 1803514.

(82) H. Y. Zheng, X. H. Dong, W. W. Wu, G. Z. Liu, and X. Pan, "Multifunctional Heterocyclic-Based Spacer Cation for Efficient and Stable 2D/3D Perovskite Solar Cells," *Acs Applied Materials & Interfaces,* vol. 14, no. 7, pp. 9183-9191, Feb 2022.

(83) H. L. Loi *et al.*, "Gradient 2D/3D Perovskite Films Prepared by Hot-Casting for Sensitive Photodetectors," *Advanced Science,* vol. 7, no. 14, Jul 2020, Art. no. 2000776.

(84) A. Krishna, S. Gottis, M. K. Nazeeruddin, and F. Sauvage, "Mixed Dimensional 2D/3D Hybrid Perovskite Absorbers: The Future of Perovskite Solar Cells?,"

Advanced Functional Materials, vol. 29, no. 8, Feb 2019, Art. no. 1806482.

(85) H. H. Tsai *et al.*, "High-efficiency two-dimensional Ruddlesden-Popper perovskite solar cells," *Nature,* vol. 536, no. 7616, pp. 312-+, Aug 2016.

(86) H. Li *et al.*, "Rapid and Reliable Thickness Identification of Two-Dimensional Nanosheets Using Optical Microscopy," *ACS Nano,* vol. 7, no. 11, pp. 10344-10353, 2013/11/26 2013.

(87) E. Belarbi *et al.*, "Transformation of PbI2, PbBr2 and PbCl2 salts into MAPbBr3 perovskite by halide exchange as an effective method for recombination reduction," *Physical Chemistry Chemical Physics,* 10.1039/C7CP01192J vol. 19, no. 17, pp. 10913-10921, 2017.

(88) Y. Miao *et al.*, "Designable Layer Edge States in Quasi-2D Perovskites Induced by Femtosecond Pulse Laser," *Advanced Science,* 2022, Art. no. 2201046.

(89) J. C. Blancon *et al.*, "Extremely efficient internal exciton dissociation through edge states in layered 2D perovskites," *Science,* vol. 355, no. 6331, pp. 1288-1291, Mar 2017.

(90) Z. J. Qin *et al.*, "Spontaneous Formation of 2D/3D Heterostructures on the Edges of 2D Ruddlesden-Popper Hybrid Perovskite Crystals," *Chemistry of Materials,* vol. 32, no. 12, pp. 5009-5015, Jun 2020.

(91) Z. Zhu *et al.*, "Interaction of Organic Cation with Water Molecule in Perovskite MAPbI(3): From Dynamic Orientational Disorder to Hydrogen Bonding,"

Chemistry of Materials, vol. 28, no. 20, pp. 7385-7393, Oct 2016.

(92) C. M. M. Soe *et al.*, "Structural and thermodynamic limits of layer thickness in 2D halide perovskites," *Proceedings of the National Academy of Sciences of the United States of America,* vol. 116, no. 1, pp. 58-66, Jan 2019.